Alma Mater Studiorum – Università di Bologna
in cotutela con Pontificia Universidad Católica de Chile

DOTTORATO DI RICERCA IN

Nanoscienze per la medicina e per l'ambiente

Ciclo 35

Settore Concorsuale: CHIM/04

Settore Scientifico Disciplinare: 03/C2

Nanocomposites based on poly(caprolactone)-chitosan electrospun nanofibers and metallic oxide nanoparticles. Their potential use to adsorption and photocatalytic degradation of organic contaminants

Presentata da: Alexander Cordoba Manrique

Coordinatore Dottorato

Prof. Dario Braga

Supervisore

Prof. Angel Leiva

Supervisore

Prof. Maria Letizia Focarete

Esame finale anno 2023

FACULTAD DE QUÍMICA Y DE FARMACIA
PONTIFICIA UNIVERSIDAD CATÓLICA DE CHILE

DEPARTAMENTO DE QUÍMICA FISICA
ESCUELA DE QUÍMICA

Nanocomposites based on poly(caprolactone)-chitosan electrospun nanofibers and metallic oxide nanoparticles. Their potential use to adsorption and photocatalytic degradation of organic contaminants

ALEXANDER CORDOBA MANRIQUE

Tesis para optar al Grado Académico de Doctor en Química.

Directores de Tesis : **Dr. Angel Leiva**
Dra. Maria Letizia Focarete

Santiago de Chile, Abril de 2023

DIRECCIÓN DE INVESTIGACIÓN Y POSTGRADO

DEPARTAMENTO DE QUÍMICA FÍSICA

Nanocomposites based on poly(caprolactone)-chitosan electrospun nanofibers and metallic oxide nanoparticles. Their potential use to adsorption and photocatalytic degradation of organic contaminants

ALEXANDER CÓRDOBA MANRIQUE

**Thesis to qualify for the Academic
Degree of Doctor in Chemistry**

**Thesis Supervisors: PhD. Ángel Leiva Campusano
PhD. Maria Letizia Focarete**

Santiago de Chile, April 2023

A mis padres
Yolanda y Alexander

Acknowledgments

I am grateful to the following entities and people who in one way or another made it possible to develop this research work fully:

To the " Agencia nacional de investigacion y desarrollo" (ANID) for the funding granted within the framework of the national scholarships for doctorates (21191257). Their support has allowed me to pursue my academic goals and conduct research in my field of interest.

To the Pontificia Universidad Católica de Chile for the "VRI ayudante" and "VRI instructor" and “apoyo a casos críticos” scholarships provided me the financial support I needed to complete my doctoral degree.

To the Alma Mater Studiorum - Università di Bologna for accept me in the co-tutelle program, which has allowed me to obtain a double degree. The university's commitment to fostering academic collaboration and excellence has been instrumental in making this achievement possible.

To PhD. Angel Leiva for his invaluable support and guidance during my research work. His direction, financial contribution, and management were instrumental to my success. I especially appreciate his understanding during difficult moments and for being a great human being and mentor.

To PhD. Letizia Focarete for her support and guidance throughout my research work. Her invaluable assistance and expertise were essential to the success of my project, and I am particularly grateful for her continued support during the pandemic.

To PhD Cesar Saldias for his invaluable support and guidance throughout my doctoral studies. Not only has he been an exceptional professor, but also a trusted friend who provided me with invaluable advice and encouragement both academically and personally. I am grateful for his support and fortunate to have worked with such an outstanding professor and friend.

To all the members of macromolecules lab, especially Vivi, Oscar, Barabara, Castillito, Pia, Alejandro, Gabriel, Pablo, Coni, for their support in the development of my formation.

To all the members of Polymer Science and Biomaterials lab: Georgia, Valentina, Mario and Elena, for their warm hospitality and kindness during my stay in Italy. They welcomed me with open arms, made me feel at home, and showed me the beauty of their country. I am deeply grateful for their friendship, which made my doctoral studies much more enjoyable and memorable.

To my second family that I created in Chile: Angie, Andres, Oriel, and Pau. Their unconditional support has been invaluable to me during difficult times. I appreciate their unwavering faith in me, and I look forward to sharing more triumphs together. Thank you for being an important part of my journey.

To all the friends and colleagues who have supported me on my journey to becoming a scientist. In particular, I would like to express my gratitude to Alejandra, Suany, Natalia, Miguel, Diana, Tulio, Mayra, Elizabeth, Nory, Wilson, Daniela, Valeria, Jackson, Sergio y any, Nico y Gaby, and many others who have provided me with encouragement, advice, and support along the way.

To Professor Gustavo Salazar for his great support, since he planted the scientific seed that it continues to grow and still does not cease to do so.

To my family, who have been my constant source of support and motivation throughout my academic journey. To my parents, Yolanda and Alexander, thank you for instilling in me the values of hard work, perseverance, and determination. Your unwavering support and encouragement have been instrumental in my success. To my simblings Javier and Angélica, thank you for being my lifelong companions, and for sharing in my joys and struggles. To my niece Alejandra and nephews Juan and Dylan, thank you for bringing joy and light into my life and for reminding me of the importance of family. I am incredibly fortunate to have such a loving and supportive family, and I am grateful for your unconditional love and guidance. Thank you for being my rock, and for always inspiring me to pursue my dreams.

To my life partners Pau and Rhem, without them none of this would have been possible. All the support I receive is infinite. Thank you for all the moments of teaching and moments of happiness and enjoyment. Pau, your influence on me has been immeasurable, you have made me a better person. And rhem, you have made me experience an unimaginable love, you came into my life just when I needed it the most. Together, we make the best family in the world, and I am honored to have you both by my side.

And finally, what makes it all possible, god.

List of Abbreviations

AOPs	Advanced oxidation processes
ATR	Attenuated total reflectance
BET	Brunauer-Emmett-Teller
BJH	Barrett-Joyner-Halenda
C	Contaminant
CB	Conduction band
CS	Chitosan
DMA	Dynamic mechanical analysis
DSC	Differential Scanning Calorimetry
E	Young's modulus
e^-	Electron
FFT	Fast Fourier Transform
FT-IR	Fourier transform-infrared
h^+	Hole
HR-TEM	High resolution transmission electron microscopy
LH	Langmuir-hinshelwood
LNCS	Liquid Nitrogen Cooling System
NFs	Nanofibers
NPs	Nanoparticles
P25	Commercial titanium oxide nanoparticles
PBI	Perylene tetracarboxylic acid bisimide
PBIJ	Perylene bisimide -jeffamine t-403
PCL	Polycaprolactone
PCL-CS NFs	Polycaprolactone-chitosan nanofibers
PCL-CS-P25 NFs	Polycaprolactone-chitosan with commercial titanium oxide nanoparticles
PCL-CS-TiO_2TX NFs	Polycaprolactone-chitosan with synthesized titanium oxide nanoparticles
PCL-P25-NFs	Polycaprolactone with commercial titanium oxide nanoparticles
RhB	Rhodamine B
S	Active sites
SC	Adsorption complex
SEM	Scanning electron microscopy
TCSPC	Time-correlated single-photon counting
TEM	Transmission electron microscopy
TGA	Thermal gravimetric analysis
TiO_2NPs	Titanium oxide nanoparticles
TiO_2TXNPs	Titanium oxide nanoparticles synthesized with triton x

TIP	Titanium Isopropoxide
UV-Vis	Ultraviolet–visible
VB	Valence band
ε_b	Elongation at break
σ_b	Strain at break

Table of contents

Index of tables

Index of figures

Abstract

Pollution of water bodies is one of the most common environmental problems today. Organic pollutants are one of the main drawbacks in this natural resource, among which the following stand out long-lived dyes, pharmaceuticals, and pesticides. This research aims at obtaining nanocomposites based on polycaprolactone-chitosan (PCL-CS) electrospun nanofibers (NFs) containing TiO_2 nanoparticles (NPs) for the adsorption and photocatalytic degradation of organic pollutants, using Rhodamine B as a model. The fabricated hybrid materials were characterized by FT-IR, TGA, DSC, SEM, TEM, tensile properties, and the contact angle of water drops. The photoactivity of the NFs was investigated using a batch-type system by following UV-Vis absorbance and fluorescence of rhodamine B (RhB).

For this purpose, TiO_2NPs were successfully ex-situ incorporated into the polymer matrix promoting good mechanical properties and higher hydrophilicity of the material. The results showed that CS in the NFs increased the absorption and degradation of RhB by the TiO_2NPs. CS attracted the pollutant molecules to the active sites vicinity of TiO_2NPs, favoring initial adsorption and degradation. In other words, a bait-hook-and-destroy effect was evidenced. It also was demonstrated that the sensitization of TiO_2 by organic dyes (e.g., perylene derivative) considerably improves the photocatalytic activity under visible radiation, allowing the use of low amounts of TiO_2. (≈0.05 g/1 g of fiber). Hence, the current study is expected to contribute with an environmentally friendly green alternative solution.

Resumen

La contaminación de los cuerpos de agua es uno de los problemas medioambientales más comunes en la actualidad. Los contaminantes orgánicos son uno de los compuestos perjudiciales más importantes, entre los que destacan los colorantes de larga vida, los productos farmacéuticos y los pesticidas. Esta investigación tiene como objetivo la obtención de nanocompositos basados en nanofibras (NFs) electrohiladas de policaprolactona-quitosano (PCL-CS) con nanopartículas de TiO_2 (TiO_2NPs) para la adsorción y degradación fotocatalítica de contaminantes orgánicos, utilizando como modelo la rodamina B. Los materiales híbridos fabricados se caracterizaron por FT-IR, TGA, DSC, SEM, TEM, propiedades de tracción y ángulo de contacto de gotas de agua. La fotoactividad de las NFs se investigó utilizando un sistema tipo “batch” seguida por espectroscopia UV-Vis y microscopia de fluorescencia.

Para este propósito, se incorporaron ex-situ las TiO_2NPs a la matriz polimérica mostrando buenas propiedades mecánicas y una mayor hidrofilicidad del material. Los resultados mostraron que la presencia de CS en las NFs aumentaba la absorción y degradación de RhB por las TiO_2NPs. El CS atrae las moléculas contaminantes a los sitios activos como las TiO_2NPs, favoreciendo la adsorción y degradación. En otras palabras, se evidenció un efecto anzuelo-y-destrucción (bait-hook-and-destroy effect). También se demostró que la sensibilización del TiO_2 mediante colorantes orgánicos (por ejemplo, un derivado del perileno) mejora considerablemente la actividad fotocatalítica bajo radiación visible, permitiendo el uso de bajas cantidades de TiO_2. (≈0,05 g/1 g de fibra). Por lo tanto, se espera que el presente estudio contribuya con una solución alternativa ecológica y respetuosa con el medio ambiente.

1. Chapter I. Introduction

Water pollution has been one of society's most dramatic problems. Organic pollutants, such as pesticides, pharmaceuticals, and dyes, have been detected in water sources worldwide. Several treatment methods have been developed to remove or separate organic contaminants from the water, such as coagulation, flocculation, electrolysis, and bacteria-guided treatments. However, some contaminants are too resistant to those strategies resulting in the concentration and transport of pollutants from place to place. For this reason, focusing on a more effective and environmentally friendly treatment that destroys contaminants has become essential.

Hence, advanced oxidation processes (AOPs) have emerged as an innovative strategy within green chemistry to degrade the main pollutants in wastewater. Such techniques may involve photocatalytic reactions that generate reactive oxygen species [1]. These short-lived reactive species are not only capable of degrading organic pollutants but also viruses and bacteria. In AOPs, semiconductor nanoparticles have been used extensively as photocatalysts due to their light-sensitive optical properties and sizeable active surface area.

Nevertheless, the disadvantageous tendency of nanoparticles (NPs) to spontaneously agglomerate reduces their effective surface area leading to a decrease in photocatalytic activity. Moreover, recovering NPs from the reaction medium for subsequent efficient reuse has also proven challenging. For these reasons, the number of studies seeking to support NPs for improved application has increased considerably. In this regard, electrospun polymeric nanofibers are a promising alternative to support and stabilize NPs. Nanofibers (NFs) display unique functional properties, such as nanometer fiber diameter, large surface area relative to their volume, tensile strength, flexibility, and options for different surface functionalities [2, 3]. Additionally, NFs can be obtained as macroscopic mat-like structures characterized by their stability, flexibility, elasticity, and porosity, favoring their use in various applications, such as tissue engineering [4, 5], drug delivery [6], optical sensors [7], and air filtration [8].

Considering all the above-mentioned aspects, a promising option to be applied in photocatalytic water remediation processes is a hybrid material based on biocompatible polymeric NFs and photoactive NPs.

One of the most promising natural polymers for this application is chitosan due to its biocompatibility, biodegradability, innocuousness, and antimicrobial activity. Chitosan is a natural polysaccharide derived from chitin, which contains numerous polar and ionizable groups that induce a high affinity with water and other interesting molecules [9, 10]. However, the high polarizability degree of chitosan imposes high forces on the jet of polymer solution during electrospinning causing instability and low processability. The use of solvents with a marked acidic character, such as trifluoroacetic acid, has improved chitosan electrospinnability [10, 11]. Alternative strategies usually use additives as a second polymer that enhances its mechanical properties.

In this regard, an ideal candidate to assist the electrospinning process of chitosan is polycaprolactone (PCL). PCL shows high miscibility with chitosan and exhibits essential characteristics such as biocompatibility, biodegradability, and harmlessness [9, 12].

Consequently, this research aims to obtain nanocomposites based on polycaprolactone-chitosan and photocatalytic nanoparticles (PCL-CS-NPs) for the adsorption and photocatalytic degradation of organic pollutants, particularly rhodamine B as a pollutant model molecule.

The proposed strategy is to take advantage of the properties of each component of the hybrid material. CS contributes to the adsorption of organic pollutants and NPs, PCL provides mechanical properties and electrospinnability, and metallic oxide NPs give photocatalytic activity to degrade the pollutants. In this way, the material obtained is expected to act through two steps: *i*) firstly, the adsorption of contaminants in aqueous media occurs over the nanofibers, and *ii*) later, the diffusion of the pollutants towards the active sites of the photocatalyst would allow their subsequent decomposition, also known as bait-hook and destroy strategy.

1.1. Electrospinning

There is a variety of techniques to obtain nanofibers: supersonic laser drawing with CO_2 [13], spinning by solution blowing [14], centrifugal jet spinning [15], direct electrodynamic drawing[16], and others[17]. However, the most established technique for producing nanofibers in a continuous form is electrospinning [9, 18]. Electrospinning was developed in the first half of the 20th century to generate fibers with small diameters, even reaching a few hundred nanometers. Its versatility has allowed the manufacture of scaffolds of numerous biodegradable polymers such as poly (caprolactone), poly (lactic acid), poly (glycolic acid), and poly (urethanes), among others [19].

The typical electrospinning assembly comprises a syringe, a collector, and a high-voltage power supply (See Figure 1). The syringe acts as a polymer solution reservoir and has a metal capillary at the tip, usually connected to the positive terminal of a high-voltage source. Whereas, the negative terminal is connected to a metal collector in order to complete the circuit. The direction of potential difference is chosen at convenience, depending on the work solution. The syringe is placed in an infusion pump to control the process flow rate. When the hemispherical shape of the drop is formed at the needle tip, it is destabilized by the charges accumulated on the surface to become a "Taylor Cone" in the presence of high voltage. The electrical forces overcome the surface tension on the drop when reaching a critical voltage. At this moment, a jet of ultrafine fibers is produced from the tip of the Taylor Cone, resulting in the formation of electrospun nanofiber mats. As mentioned above, these materials exhibit interesting characteristics, such as stability in different media, high surface area per unit mass, and good mechanical strength [10].

1.2. Chitosan-polycaprolactone nanofibers

One of the most promising natural polymers is chitosan (CS). Its biocompatibility, biodegradability, hydrophilicity, non-toxicity, and antimicrobial activity make it an ideal candidate for environmentally friendly applications[20]. CS would present different advantages over other materials used in water remediation technologies due to its environmental friendliness. In addition, CS has numerous polar and ionizable groups inducing a great affinity with water (See *Figure 2*, a). Possible applications of this material in separation technologies as new nanofiber membranes for fine filtration and neutralization

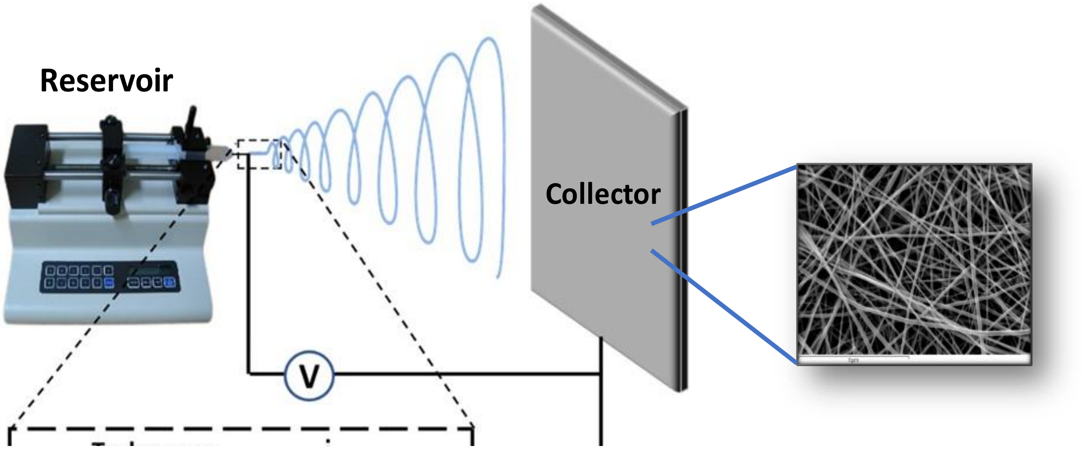

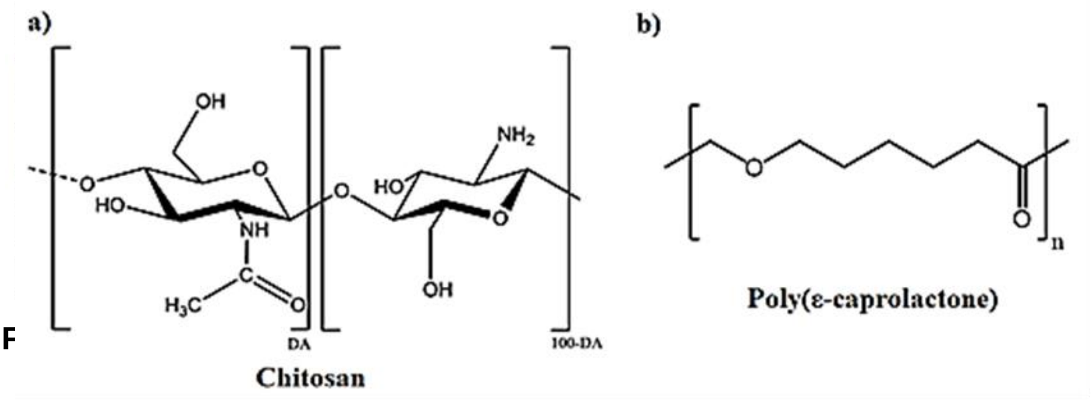

F

Figure 2. Chemical structure of a) Chitosan and b) Poly (ε-caprolactone). *DA: degree of N-acetylation

of metals and toxic microbes have been reported [9, 10]. CS has garnered significant attention as a promising material for supporting metallic nanoparticles. Its ability to attract and reduce metal ions as well as cap and stabilize the resulting nanoparticles makes it an ideal candidate for the controlled synthesis of metallic nanoparticles [21-23]. The amine and hydroxyl groups in chitosan molecules exhibit strong complexation abilities with metal ions, which contributes to its suitability as a support material [21-23]. Additionally, the surface structure of chitosan has been found to play a critical role in retaining nanoparticles [24]. Recent studies have highlighted the potential of chitosan as a carrier for various nanoparticles, including silver, gold, platinum, and palladium nanoparticles [21-24].

In 2004, Ohkawa and coworkers prepared pure CS fibers for the first time using the electrospinning technique [25]. Hydrochloric acid, formic acid, and trifluoroacetic acid were tested as possible solvents, and trifluoroacetic acid gave the best results. The authors also observed that adding dichloromethane to the system improved the homogeneity of the fibers [25]. Usually, to overcome the inherent poor processability of CS, another substance that improve the mechanical properties of nanofibers, such as poly (caprolactone), poly (ethylene oxide), poly (vinyl alcohol), cellulose, zein, poly (lactic acid), nylon-6, among others, must be added [9, 19, 26].

In this regard, a good aide to CS is poly(caprolactone) (PCL) due to its similar properties, such as biocompatibility, biodegradability, non-toxicity, and its good mechanical properties (Figure 2,b). This aliphatic polyester shows high miscibility with several polymers improving its processability, particularly CS [9, 12]. PCL-CS nanofiber electrospinning has shown promising potential for biomedical applications [9]. Notably, while more hydrophilic is a scaffold, this exhibits a better connection whit cells, which provides a possible application in tissue engineering [27, 28].

Due to the opposite hydrophilicity between PCL and CS, it is difficult to achieve a single solvent that solubilizes both polymers. The amines and hydroxyl groups in the CS backbone not only provide hydrophilicity but also give weak basicity [19]. For this reason, different solvents have been used to take advantage of this characteristic in the CS / PCL mixture, such as trifluoroacetic acid, hexafluoro-2-propanol, formic acid-acetone [19], and acetic acid-formic acid [9].

Some investigations about applications of a tricomponent material, PCL/CS/Nanoparticles (PCL/CS/NPs), have been reported. For example, Wu and coworkers synthesized PCL/CS nanofibers with hydroxyapatite nanoparticles and tested them in vitro experiments with osteoblastic cells to regenerate tendons and ligaments [29]. Rijal and coworkers obtained PCL/CS/MgO for use in tissue engineering, such as bone regeneration, drug release, and wound healing by virtue of its non-toxicity and biocompatibility [30]. Wang and coworkers modified the surfaces of PCL/carbon nanotubes nanofibers with CS by electrostatic attraction, demonstrating that CS can improve adhesion and cell proliferation over the fibers and provide antibacterial activity against E. coli and S. aureus for biomedical applications [31]. Among other studied systems are mixtures type PCL/CS/Gelatin [32], PCL/CS coaxial NFs with silver nanoparticles [33], PCL/CS/ Hydroxyapatite doped with Zn [34]. In this regard, research has also been conducted on PCL/CS/NPs systems for the degradation of several pollutants. For example, using nickel NPs in the reduction catalysis of nitro phenols in the presence of sodium borohydride as a reducing agent [35]. Alternatively, Lee and coworkers synthesized nanofibers of polyvinylpyrrolidone and poly(vinylidene fluoride) with TiO_2 NPs for the degradation of methylene blue [36]. In turn, Salama and coworkers synthesized cellulose acetate nanofibers with carbon nanotubes and TiO_2 nanoparticles for the degradation of indigo carmine and methylene blue [37].

1.3. Photocatalysis with a nanostructured semiconductor

Photocatalysis is one of the most promising strategies for developing inexpensive and eco-friendly solutions for many environmental issues. The approach has been so remarkable because the pollutants can be converted into safe compounds, and solar light is a nonhazardous, sustainable energy source.

In recent decades, the use of nanoparticles (NPs) of different natures, such as ZnO, Cu, CuO, TiO_2, Au, Ag, Pd, Pt, and Ni, in photocatalysis has been reported [35, 38-42]. However, undoubtedly semiconductors are the materials most widely used in photocatalysis.

When a semiconductor absorbs a photon of proper energy, an exciton is formed. An exciton is a bounded state of an electron promoted to the conduction band (CB) and an electron-hole left in the valence band (VB), which is mediated by electrostatic forces, Figure 3 [43]. After its formation, the exciton may undergo both radiative and nonradiative processes, such as in molecular photophysics. Both radiative and nonradiative charge recombinations can be exploited in different applications and are governed by strict conservation rules.

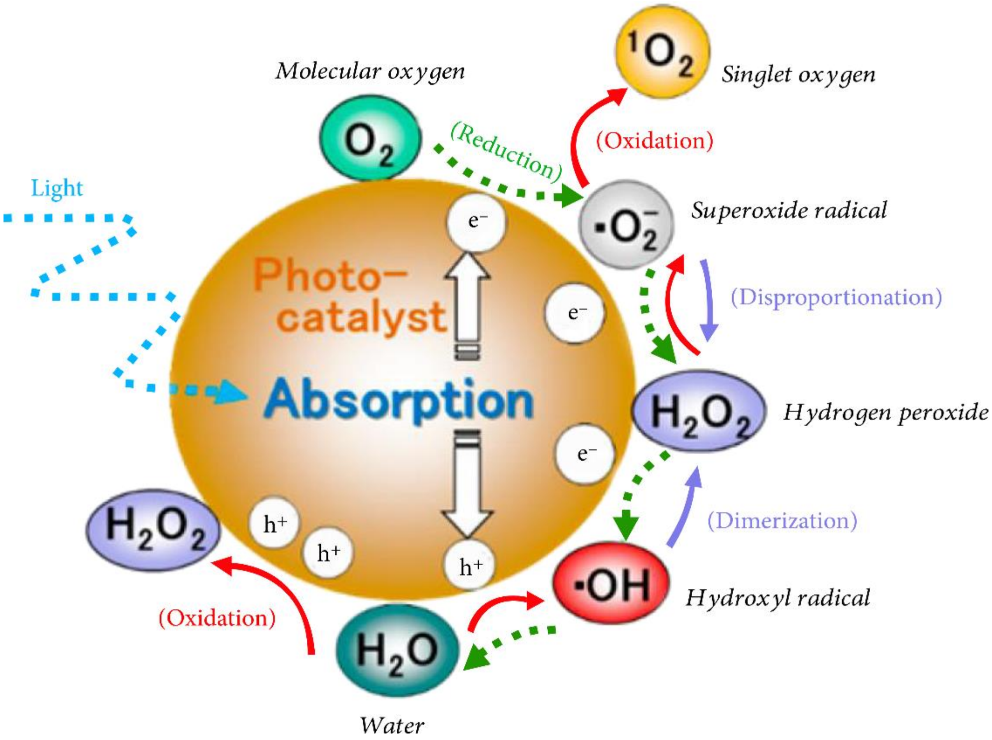

Figure 3. Fundamental steps in photocatalysis. Reprinted with permission from [43]

In a light-mediated advanced oxidation process, the photogenerated electron in CB moves towards the surface, and it is scavenged by oxygen in the medium to generate the superoxide anion $O_2^{\cdot -}$. Later, $O_2^{\cdot -}$ can become the radical HOO· by rapid protonation; simultaneously, the h^+ in the VB migrates through NP surface and reacts with both H_2O and OH^- ions to produce active species such as OH·. It is important to note that the process's efficiency can be attributed to the efficient separation of photogenerated e--h+ pairs. Thus, the active oxygen species ($O_2^{\cdot -}$, HOO·, OH·) are responsible for degrading organic molecules into less harmful minerals or organic compounds [44-46] (See Figure 3). The possible mechanism described above can be summarized as follows:

$$\mathrm{NP} + h\nu \longrightarrow \mathrm{NP}(h^+) + \mathrm{NP}(e^-) \tag{1}$$

$$e^- + \mathrm{O_2} \longrightarrow \mathrm{O_2^{\bullet -}} \tag{2}$$

$$\mathrm{H_2O} + \mathrm{O_2^{\bullet -}} \longrightarrow \mathrm{OOH^\bullet} + \mathrm{OH^-} \tag{3}$$

$$2\mathrm{OOH^\bullet} \longrightarrow \mathrm{O_2} + \mathrm{H_2O_2} \tag{4}$$

$$\mathrm{H_2O} + h^+ \longrightarrow \mathrm{OH^\bullet} + \mathrm{H^+} \tag{5}$$

$$\mathrm{OH^-} + h^+ \longrightarrow \mathrm{OH^\bullet} \tag{6}$$

$$\boldsymbol{CO} + h^+ \longrightarrow \boldsymbol{CO}^+ \tag{7}$$

$$\boldsymbol{CO}^+ + (\mathrm{O_2^{\bullet -}}, \mathrm{OOH^\bullet}\ \mathrm{o}\ \mathrm{OH^\bullet}) \longrightarrow \begin{array}{c}\text{Peroxy or}\\ \text{hydroxylate}\\ \text{intermediate}\end{array} \longrightarrow \text{Degraded products} \tag{8}$$

For their use, most of these nanoparticulate materials whit catalytic activity is dispersed in water, so their recycling becomes difficult. In this condition, materials easily agglomerate and lose their activity due to photo-corrosion. For these reasons, methods of particle coating or the immobilization of nanopowders to their stabilization have been used, avoiding agglomeration and improving the rate of reuse and photocatalytic activity. Among the most used stabilizer agent are polymers, which have significant advantages such as great diversity in nature, size and shape, a more straightforward and easier scalable synthesis procedure, and simple convenient recycling processes [47].

1.3.1. Titanium dioxide: structural and photocatalytic properties

Titanium oxide (titania, titanium (IV) oxide) is the most abundant oxide of titanium in nature [48], having formula TiO_2. Most of it is produced from ores containing ilmenite, rutile, anatase, and leucoxene, which are massively mined from deposits scattered throughout the world and purified by the so-called "chloride" or "sulfate" process [49]. In the "chloride" process, the ore is treated with chlorine and active carbon to obtain titanium tetrachloride, which could be purified by distillation and then treated with oxygen to obtain the final product. In the "sulfate" process, ilmenite ores are purified by the addition of sulfuric acid, which could remove Fe(II) ion forming the respective sulfate salt and giving synthetic rutile

The three most common titanium dioxide crystalline forms are rutile (most abundant), anatase, and brookite. They can be visualized as distorted octahedral configurations, having as octahedrons a titanium atom surrounded by six oxygen atoms, see Table 1.

Table 1. Parameters of titania crystalline forms

Crystal Form	Density(g/cm^3)	Crystal System	Unit Cell (A)
Rutile	4240	Tetragonal	a=4.5937, c=2.9587, Z=2
Anatase	3830	Tetragonal	a=3.7845, c=9.5143, Z=4
Brookite	4170	Rhombohedral	a=5.4558, b=9.1819, c=5.1429, Z = 8

Rutile is thermodynamically the most stable polymorph of TiO_2, while anatase and brookite resulted in metastable phases. Thanks to the lower energy surface, anatase tends to be the kinetically favored polymorph during many processes. Rutile and anatase show different bandgap energies (3.1 eV and 3.2 eV, respectively [50]) and anatase shows greater photoreactivity under UV irradiation than other crystalline forms.

The photocatalytic properties of titanium dioxide (anatase phase) nanosystems under UV irradiation have been well-known since 1967 [51]. Since then, titanium dioxide has been considered a promising material in photocatalysis. It has also withdrawn much interest thanks to its higher photoreactivity compared with other inorganic semiconductors [52, 53], its photostability, and the fact that it is inexpensive. However, titania photocatalytic properties are dramatically limited by fast electron-hole charge recombination, which limits the maximum theoretical photonic efficiency to 10% [54].

The photocatalytic performance of titanium dioxide is extensively related to surface properties: first, surface defects enhance photoreactivity, and second, photoredox reactions consist of interfacial charge transfer reactions at the photocatalyst surface. For these reasons, TiO_2 nanosystems development has resulted in a promising and smart strategy for improving TiO_2 photoactivity [52, 55].

As described for the catalytic activity of TiO_2, the photocatalytic reaction of TiO_2NPs starts when they absorb the energy from the radiation source. The photonic excitation then leaves the valence band unfilled, creating the electron-hole pair (e^--h^+). Excited electrons in the conduction band can flow to or from the absorber, allowing the formation of both positively and negatively charged species on the surface [56]. In general, the following mechanism is accepted for photocatalytic degradation of pollutants in aqueous media [56-60]:

Excitation

$$TiO_2 + h\nu \rightarrow e^-_{CB} + h^+ \qquad \text{(a)}$$

Charge carrier trap

$$h^+_{VB} + TiO^{IV}OH \rightarrow [TiO^{IV}OH\,\cdot]^+ \qquad \text{(b)}$$

$$e^-_{CB} + TiO^{IV}OH \leftrightarrow [\mathrm{Ti^{III}OH}] \qquad \text{(c)}$$

$$e^-_{CB} + Ti^{IV} \rightarrow \mathrm{Ti^{III}} \qquad \text{(d)}$$

$$\mathrm{Ti^{III}} + O_2 \rightarrow Ti^{IV}O_2^-\,\cdot \qquad \text{(f)}$$

Charge carrier recombination

$$h^+_{VB} + [Ti^{III}OH]_{Surf} \rightarrow Ti^{IV}OH \qquad \text{(g)}$$

$$e^-_{CB} + [TiO^{IV}OH\,\cdot]^+ \rightarrow Ti^{IV}OH \qquad \text{(h)}$$

Hydroxyl attack

$$[TiO^{IV}OH\cdot]^{+} + R_{ads} \rightarrow Ti^{IV} + R\cdot_{ads} \tag{i}$$

$$\mathrm{OH}\cdot + R_{ads} \rightarrow R\cdot_{ads} \tag{j}$$

$$[TiO^{IV}OH\cdot]^{+} + R \rightarrow Ti^{IV} + R\cdot \tag{k}$$

$$\mathrm{OH}\cdot + R \rightarrow R\cdot \tag{l}$$

$$R\cdot + h^{+} \rightarrow R\cdot^{+} \rightarrow\rightarrow\rightarrow Degraded\ products \tag{m}$$

Superoxides

$$Ti^{IV}O_2^{-}\cdot + (H^{+}) \leftrightharpoons Ti^{IV}(HO_2\cdot) \tag{n}$$

$$e^{-} + Ti^{IV}(HO_2\cdot) + (H^{+}) \leftrightharpoons Ti^{IV}(H_2O_2) \tag{o}$$

$$(H_2O_2) + (OH\cdot) \leftrightharpoons (HO_2^{-}\cdot) + (H_2O) \tag{p}$$

Where R represents the contaminant molecule.

One of the main problems of photocatalytic reactions is electron-hole recombination which results in the quenching of excitons directly affecting photodegradation reaction performance. The electrons trapped on the surface undergo fast recombination (10 ns)(equation g), while the recombination of holes is much slower (100 ns) (equation h). Recombination can be avoided if these species are separated and subsequently trapped by adsorbates on the surface or by other sites. The main hole traps are commonly hydroxyl ions or water molecules, while e- can be trapped by dissolved oxygen. In this sense, the presence of water is indispensable in TiO_2 photocatalysis [58].

Equation b describes the oxidation of OH^- ions on the TiO_2 surface by h+, generating hydroxyl radicals. Immediately after this reaction, the hydroxyl radical is still associated with TiO_2. So hydroxyl radicals could react, both attached to the surface and in the site vicinity by diffusion into the medium [57]. The four possible reaction cases for hydroxyl radicals with contaminant molecules (R1), depending on whether they are adsorbed or not on the TiO_2 surface, are shown in reactions i-l.

Equation f shows how the presence of oxygen prevents the recombination of the e^--h^+ pair while allowing the formation of superoxide radicals $O_2\cdot^-$, which can protonate to form the hydroperoxyl radical (HO_2^-) and subsequently into H_2O_2 as shown in equations o and p, respectively [60]. The hydroperoxyl radicals formed also have the property of removing an e^-; thus, O_2 generates a double extension in the h^+ lifetime [58]. Recent studies have even revealed that superoxide radicals can sometimes replace hydroxyl radicals in favorability in the reaction mechanism involving photocatalytic degradation [59].

In addition, nanosystems implementation in different matrixes, such as electrospun nanofibers, has shown promising results [36, 61], solving the issues related to nanoparticle recovery from purified aqueous media.

Finally, improving TiO_2 spectral response to visible region has drawn increasing interest over the years [62, 63]. UV light is only a small fraction of the solar spectrum, further limiting photocatalyst performances. In order to solve this drawback, different strategies have been developed, but one of the most promising results consists of photocatalyst functionalization with a visible light sensitizer. The perylene bisimides family has shown promising results since its photostability and outstanding photochemical and photophysical properties.

1.3.2. Perylene bisimide molecules

Perylene tetracarboxylic acid bisimide colorants (PBI) have been studied and have received significant attention in academic and industrial dye research since 1950 [48]. Many PBI molecules have been used in several high-level industrial applications as a dye (such as in automotive) thanks to their excellent thermal and chemical stabilities [49]. During the last decades, PBI molecules have also found novel applications in electronic and photovoltaic materials, where they are considered the best n-type semiconductors available [64]. This outstanding success is related to PBI high electronic affinity and their interesting and unique redox and stability properties.

Furthermore, PBI molecules have also exhibited incredible potential thanks to their unique optical properties, such as high fluorescence quantum yield and photostability, which have drawn a great deal of interest in the field of novel light-induced energy and electron transfer processes [65].

In addition to their interesting single-molecule properties, PBI also exhibits the ability to organize in self-assembly supramolecular structures with complex architecture [48, 66]. These supramolecular systems show different properties compared with single molecules (e.g., more efficient energy or electron transfer phenomena have been observed), and the aggregation took place thanks to the π- π interactions between PBI molecules which resulted in being strongly solvent-dependent [67]. For example, in the presence of water, the hydrophobic effect favors the formation of supramolecular structures, while in organic solvents, such as dichloromethane, PBI behaves as single molecules. The ability to tune the supramolecular architecture allows us to tune also other properties, resulting in a promising strategy for developing novel and intriguing nanosystems.

1.4. Hypothesis

The main hypothesis of this work is the following: It is possible to obtain a nanocomposite and hybrid material based on polymeric nanofibers containing photocatalytic nanoparticles, that have a good performance as photocatalysts for remediation of water contaminated with photodegradable organic compounds.

Due to their chemical functionality it is also possible to hypothesize that the chitosan and polycaprolactone proposed for the preparation of polymeric nanofibers should be able to generate good support for TiO_2 nanoparticles. In this area, it is reasonable to expect that CS will contribute to the retention of nanoparticles on the surface of the nanofibrous material and contribute to the adsorption capacity of contaminants. While PCL mainly improves the final material's mechanical properties, allowing the formation of suitable and reproducible nanofibers. On the other hand, TiO_2 NPs will provide photocatalytic activity for the degradation of pollutants.

Consequently, all the material components are expected to contribute to the photocatalytic performance of the nanocomposite.

1.5. Objectives

1.5.1. General objective

The main objective is to produce nanocomposites with photocatalytic capability, based on electrospun polycaprolactone-chitosan nanofibers and titanium oxide nanoparticles and to study their potential use in the adsorption and photocatalytic degradation of organic pollutants.

1.5.2. Specific objectives

- To obtain PCL-CS nanofibers by electrospinning and evaluate the optimal conditions for their formation, including the selection of the appropriate solvent and determining and optimization of other experimental parameters such as polymer concentration, voltage, and needle-collector distance.
- To establish a method for obtaining titanium dioxide nanoparticles capable of conferring photocatalytic activity to the electrospun material, and ensure embedding on the nanofibers.
- To obtain and characterize PCL-CS nanofibers in the absence and presence of the TiO_2NPs.
- To study the adsorption process of organic pollutants by electrospun NFs, using rhodamine B as model compound.
- To study the photoactivity of electrospun materials by photocatalytic degradation of rhodamine B.

2. Chapter II. Experimental section

2.1. Materials

Chitosan (Medium molecular weight, 75-85 % deacetylated) and PCL ($\bar{M}n$ 80,000 g mol^{-1}) were supplied by Sigma Aldrich. Formic acid (Sigma Aldrich, 98%), acetic acid (Sigma Aldrich, 99.8%), titanium isopropoxide (TIP, Sigma Aldrich, >98%), hydrochloric acid (HCl, Sigma Aldrich, 37%), Rhodamine B (RhB, Merck) were used. All reagents, solvents and chemicals were used without further purification unless otherwise stated. Ultrapure water was produced with a Millipore system (higher than 18.2 MΩcm resistivity).

2.2. Preparation of titanium dioxide nanoparticles

Synthesis of titanium oxide nanoparticles was carried out using the sol-gel method assisted by a surfactant, Triton X-100 [68]. In a 100 mL round-bottomed flask, 0.5 g of Triton X-100, 50 mL of double-distilled water, and 0.335 g of concentrated HCl (37%) were added and stirred until a clear solution was obtained at 60 °C. At this point, 3.35 g of TIP (98%) was added under vigorous stirring (1100 rpm). A white precipitate was observed, and the agitation was brought to 600 rpm. After 48 h, a clear colloidal dispersion was obtained. The colloidal solution was purified by dialysis (exclusion of MW 10-12 kDa) against Milli-Q water for three days. A clear gel obtained was dried in an oven at 45 °C, obtaining a yellow powder as the final product. The nanoparticles obtained labelled TiO_2TXNPs were analysed by UV-Vis, TEM and HR-TEM.

2.3. Preparation of nanofiber matrix

Different polymer concentrations in a mixed acetic acid: formic acid solvent (1:1 v) were tested in order to obtain homogeneous and bead-free NFs. The concentration of PCL was expressed as weight percentage (wt%) in the solution, while the amount of chitosan was expressed as a ratio of PCL (PCL:CS).

Optimal working conditions were obtained with 6 wt% PCL and using a CS ratio of 90:10 (PCL:CS). 5 wt% (With respect of total mat weight) of TiO_2NPs commercial and synthesized in the laboratory was used to obtain reproducible electrospun samples.

In the general procedure, dry TiO_2 NPs were ultrasonicated in a mixed acetic acid: formic acid solvent (1:1 v) for 30 min. Subsequently, the appropriate amount of PCL and CS for each assay was added to the prepared dispersion and left under stirring for two more hours. This dispersion was then used for the electrospinning process.

A single needle apparatus (Spinbow Lab Unit, Spinbow S.r.l. Italy) was used for electrospinning. The polymer solution was supplied at a flow rate of 0.6 mL/h, through a PTFE tube and a 24 G needle. A grounded aluminum plate positioned 12.5 cm from the needle tip acted as a collector. Electrospinning was carried out at room temperature (22 ± 5 °C) and relative humidity of 35 ± 5 %.

2.4. Characterization of the electrospun mats

2.4.1. Analysis of surface morphology

The morphology of the electrospun NFs was examined in a Leica / Cambridge Stereoscan 360 scanning electron microscope (SEM). Before SEM measurements, the samples were coated with a gold layer using a sputtering coater. Fiber diameter distribution was determined by measuring about 400 fibers in the SEM images using Image-J software. The morphology of TiO_2NPs on polymeric NFs was observed by transmission electron microscopy (TEM) using a Philips microscope with an accelerating voltage of 80 kV. For this purpose, the fibers were electrospun directly on a 100 mesh TEM copper grid.

2.4.2. Thermal analysis

Differential Scanning Calorimetry (DSC) measurements were carried out using a TA instruments Q100 DSC equipped with a Liquid Nitrogen Cooling System (LNCS) accessory. Scans were performed from -90 to 150 °C in a nitrogen atmosphere at 20.00 °C/min. Two cooling cycles were performed: (1) controlled cooling at 10°C/min and (2) a quench cooling.

Thermogravimetric analyses (TGA) were carried out using a TGA Q500 analyzer (TA instruments) from room temperature to 600 °C at 10 °C/min under a nitrogen atmosphere. The composition can be determined by comparing the residual weights at 600 °C of the different NFs mats of the mixtures. For this, the following linear system was used:

$$\sum_i Rt(\%)_i^0 \cdot Wf_i^{Blend} = Rt(\%)_{Blend} \qquad \text{Equation 1}$$

$$\sum_i Wf_i^{Blend} = 1 \qquad \text{Equation 2}$$

Where Rt $(\%)_i^0$ represents the residual weight percentage of the i-th component, Wf_i^{Blend} is the weight fraction of the i-th component in the blend, and Rt $(\%)_{blend}$ is the residual weight percentage of the electrospun mat with all components.

2.4.3. Fourier transform infrared spectroscopy analysis

The chemical nature of the materials was analyzed by Fourier transform infrared spectrometry (FT-IR) using a Spectrum Two instrument with an attenuated total reflectance (ATR) accessory (Perkin-Elmer). FT-IR spectra were taken in the 4000-400 cm^{-1} range with a resolution of 4 cm^{-1}, accumulation of 16 scans and a step increment of 1 cm^{-1}.

2.4.4. Mechanical characterization

The mechanical properties were determined using a TA Instrument DMA Q800 on rectangular sheets cut from the electrospun mats. The samples were cut 5 mm wide and 50 mm long. The thickness of each sample was measured using a digital micrometer. Measurements were carried out in tension mode at a single strain rate of 5 mm/min at room temperature. Load-displacement curves were obtained and converted to stress-strain curves. At least five replicates were run for each specimen, and the results were reported as an average value with its corresponding standard deviation.

2.4.5. Determination of contact angle

Static contact angle measurements were performed using a KSV's CAM 100 under ambient conditions. Lateral profiles of deionized water droplets were recorded for subsequent image analysis. Five droplets were observed in different areas of each electrospun mat and the results were reported as an average value with its corresponding standard deviation.

2.5. Evaluation of Rhodamine B adsorption

The adsorption capacity of the electrospun materials was carried out in a batch-type system. For this purpose, 2 cm^2 mat (~3 mg) was immersed in 20 mL of a pollutant solution at 1 mg/L under constant agitation. The whole experiment was performed in total darkness, and the concentration of the contaminant over time was monitored by UV-Visible spectroscopy using an Agilent Cary 60 spectrophotometer. The NFs of PCL, PCL-CS, PCL-CS-P25 and PCL-P25 were confronted with observing their effect on the adsorption of the contaminants.

2.6. Evaluation of photocatalytic activity

Before the photocatalytic activity studies, light penetration into the electrospun mats was tested using a lux meter, where a decay in light intensity from 91 to 18 W/m^2 was observed, i.e., about 20 % of the light is able to pass through the material to the other side, indicating good penetration of light into the material.

Subsequently, to study the photocatalytic activity of the electrospun mats, rhodamine B (RhB) was used as a model pollutant. The activity was evaluated by means of two methods: the first consisted of continuing with the same batch system as in section 2.5 and initiating the photocatalytic reactions by irradiation with white light generated by LEDs (see emission spectrum in Figure 4). The variation of rhodamine concentration was monitored over time by UV-Vis spectroscopy (λ_{max}= 560 nm). The NFs of PCL, PCL-CS, PCL-CS-P25 and PCL-P25 were compared to observe their effect on degradation.

The second method followed the photodegradation through fluorescence microscopy, studying the decoloration of RhB against two sources of radiation; UV light (LED 365 nm) and blue light (LED 460 nm). For this purpose, a 1 cm^2 piece mat was immobilized on a glass slide, using a double-sided adhesive tape that served as a fixative and spacer for the samples. An adhesive frame was fabricated to adhere and stretch the mat's edges on the slide while providing a controlled and closed environment with a second slide placed on top of the sample; Figure 5 b shows the experimental setup. Ten µL of rhodamine at 2x10^{-5} M was added to the stretched mat surface prior to the application of the second slide.

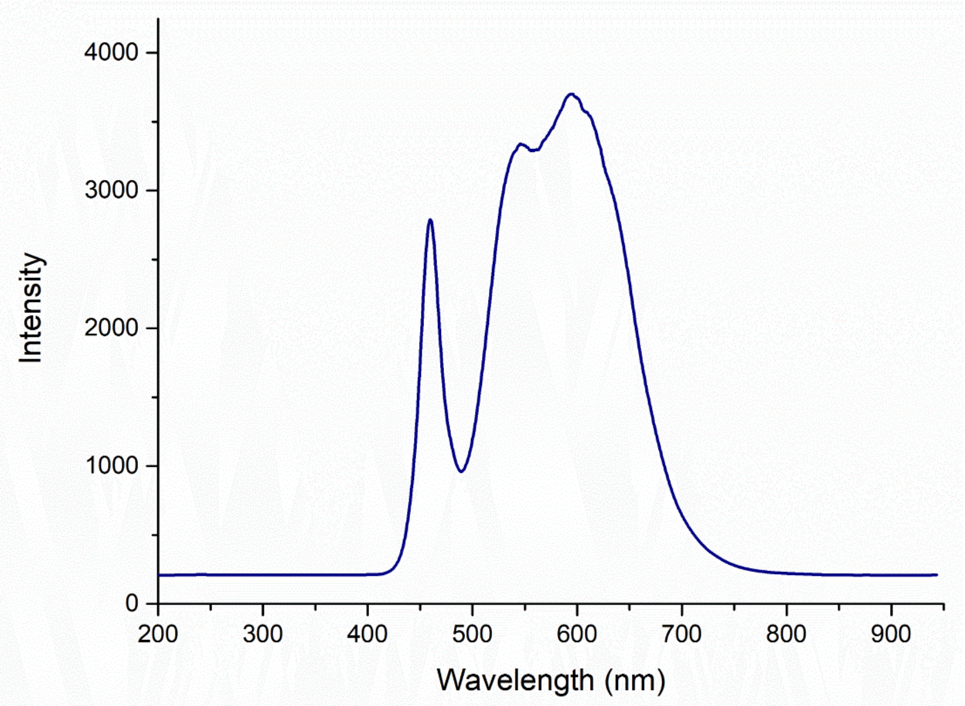

Figure 4. Emission spectrum of white LED light used for RhB photodegradation in the presence of electrospun NFs.

The RhB degradation was monitored using a modified fluorescence microscope. The experiments consisted of two stages: i) irradiation stage and ii) detection stage. During the irradiation stage, the light source is turned on for a given time (10 s for UV, and 30 s for blue). During this step, no image is acquired, and the detection light source is turned off. In the detection step, the irradiation light source is turned off, and the image is acquired using the detection light source Figure 5,c), following a classical fluorescence microscopy experiment. In this way it was possible to monitor the decoloration of RhB on the mats after each irradiation step. An example of the series of images obtained is shown in Figure 6.

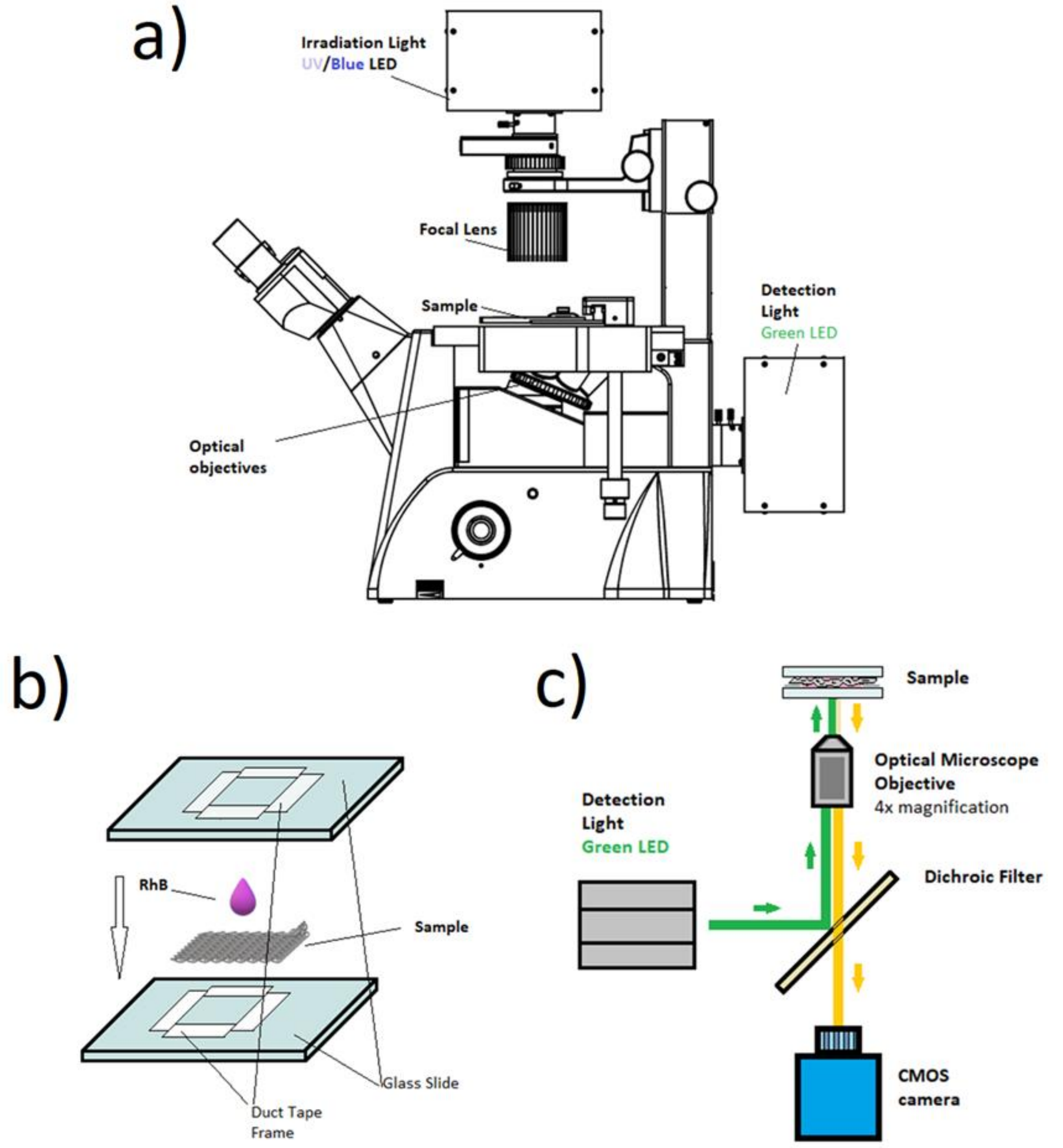

Figure 5. Schematics of the experimental setup for monitoring RhB decoloration in electrospun materials. a) Modified fluorescence microscope. b) Arrangement of RhB electrospun material between two slides. c) Detection stage setup.

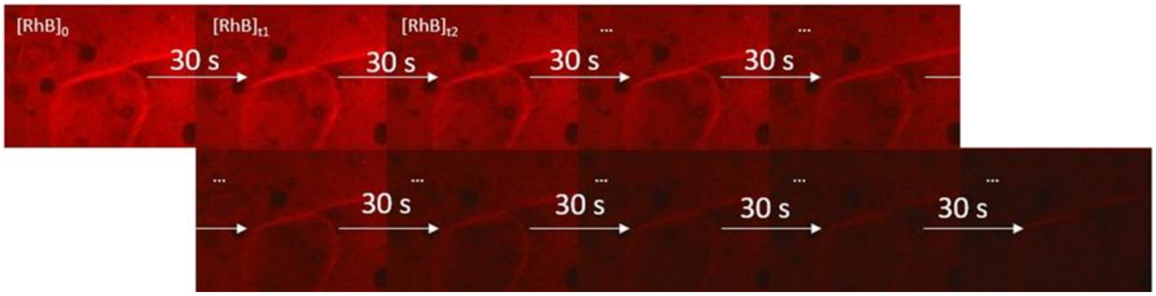

Figure 6. Example of a series of images acquired during a photodegradation experiment. In each image, it can be clearly seen that the RhB fluorescence signal decays at each step after 30 s of irradiation with blue light.

2.7. Evaluation of the use of a sensitizer

The photocatalytic study included the determination of the effect of the use of perylene bisimide -jeffamine t-403 (PBIJ) (Figure 7) as a photosensitizer on the catalytic activity of the electrospun mats. For this purpose, a 100 ppm solution of PBIJ was used as a solvent for the polymers mix. The obtention and characterization of electrospun mats were carried out as described in sections 2.2 and 2.3.

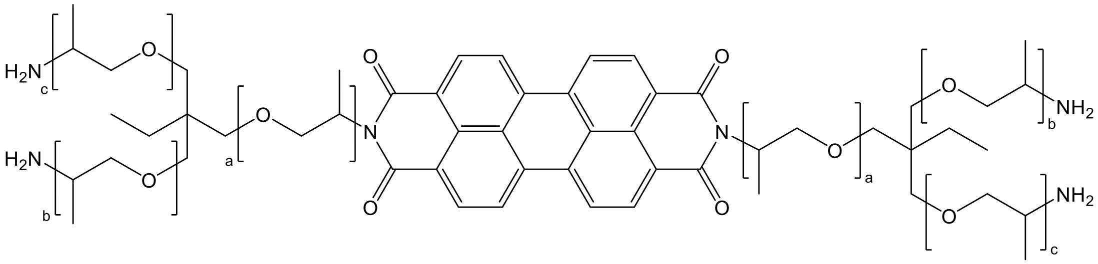

Figure 7. Chemical structure of PBIJ

3. Chapter III. Results and discussion

3.1. Characterization of the synthesized titanium oxide nanoparticles.

Figure 8 (A) displays SEM images of TiO_2NPs synthesized through a sol-gel method assisted by a triton-X surfactant. The images reveal small, irregularly-shaped particles arranged in chain-shaped aggregates. To determine particle size, an equivalent sphere diameter was used, yielding an approximate distribution (see Figure 8 (A)). The mean particles size was 6 nm with a full width at half maximum of 5 nm.

Figure 8 (B) displays high resolution TEM image of the nanoparticles alongside their corresponding Fast Fourier Transform (FFT) pattern. This image confirm that the nanoparticles possess a crystalline structure, featuring the characteristic crystal lattice of the anatase phase. Notably, the FFT pattern exhibits a distinctive [1,1,1] anatase TiO_2 pattern.

In Figure 8 (C), it can observe the absorbance spectrum of TiO_2TXNPs and the commercial TiO_2NPs (P25) for comparison. TiO_2TXNPs exhibit a reduced scattering effect and an enhanced absorbance when compared to P25. This can be attributed to the composition of P25, which consists of a combination of anatase and rutile phases. The rutile phase has an absorbance closer to blue, which generates a broader absorbance band, unlike TiO_2TXNPs, which only contain the anthase phase.

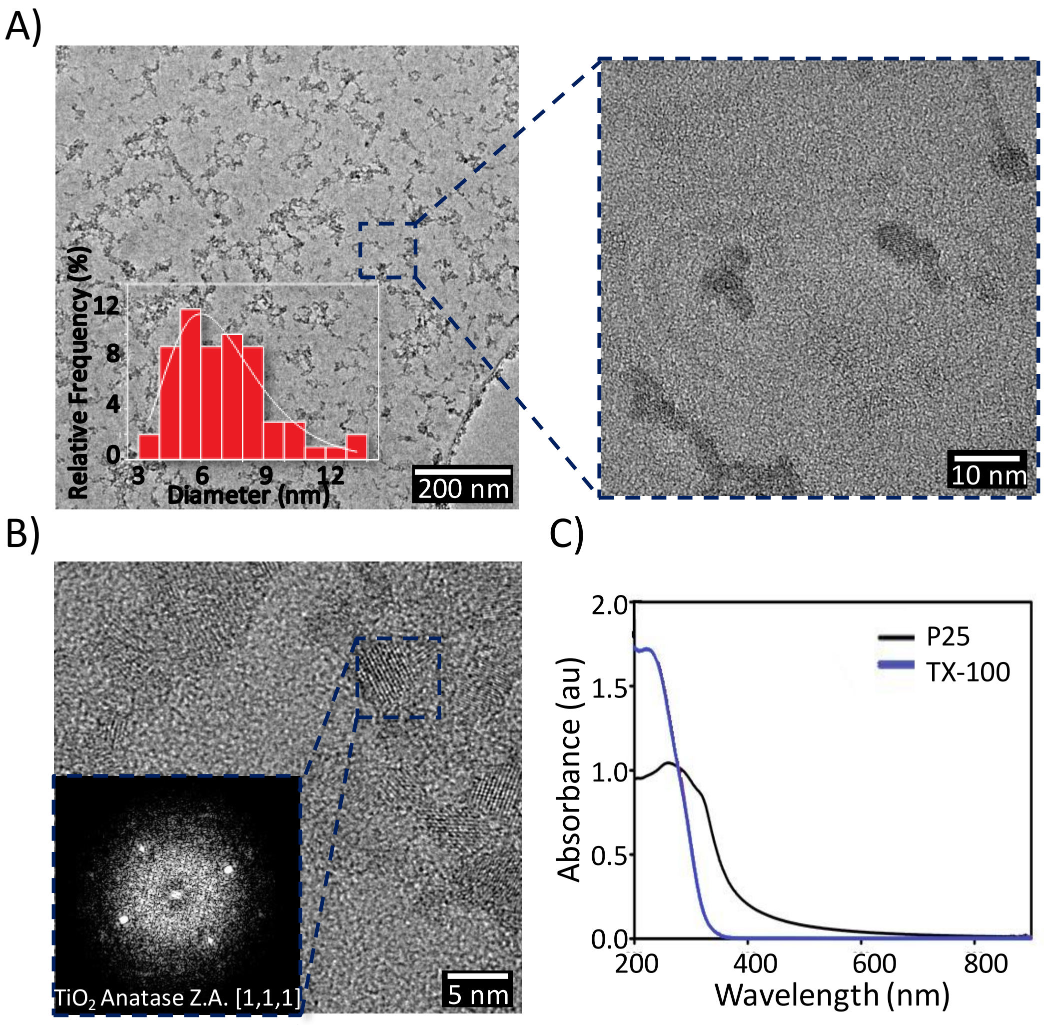

Figure 8. SEM images of TiO$_2$TXNPs and its particle diameter distribution. B) High-resolution TEM image of TiO$_2$TXNPs exhibiting anatase pattern. C) Absorbance UV-vis spectrum of TiO$_2$TXNPs and P25.

3.2. Characterization of the electrospun mats

The first step was the optimization of electrospinning parameters of PCL-CS and PCL-CS-TiO$_2$NPs. The initial optimization included a systematic adjustment of the experimental parameters: solution concentration, flow rate, working distance, and electrospinning voltage in order to obtain continuous, uniform, and bead-free nanofibers. Figure 9 shows a scheme with the main conditions tested, in addition to the result of its processability. Electrospinnability is defined as the ability to obtain homogeneous, bead-free, and reproducible formation of NFs using the studied conditions.

Reproducibility was assessed by Taylor cone formation at the needle tip and stable ejection of a single jet. Figure 9a shows the pathway followed, starting with a PCL solution at 8% by weight and varying the PCL:CS ratio from 90:10 to 80:20. The solution with the higher CS ratio presented a too high viscosity, which prevented carrying out the electrospinning process. For the other two CS ratios, the viscosity turned out to be lower, which allowed electrospinning to be performed at different voltages and flow rates. However, both solutions presented very low jet stability and practically absence of Taylor cone, leading to very low reproducibility. As an example, Figure 10a-f shows some fibers obtained under these conditions.

All tests were repeated when the PCL concentration was decreased to 6%wt, as shown in Figure 9b. In these cases, it was seen that the decrease in viscosity of the solutions substantially improved their processability.

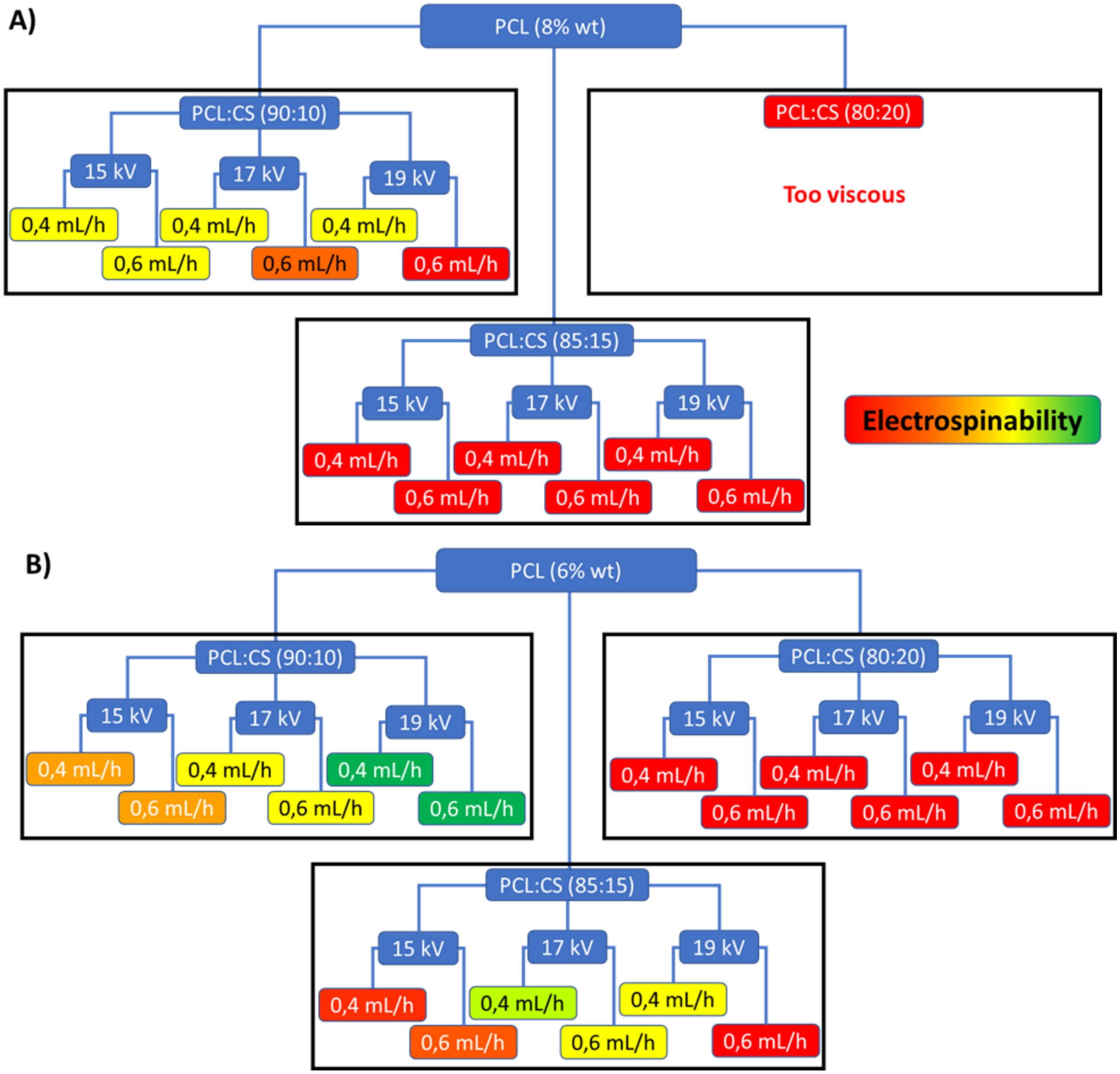

Figure 9. Schematic of the main tests performed at different conditions: PCL concentration, PCL:CS ratio, voltage and flow rate. PCL concentration A) 8% wt B) 6% wt. The color of the cell represents the electrospinability to form NFs, from the impossibility of obtaining NFs (red) until an adequate obtaining and reproducibility of NFs (green).

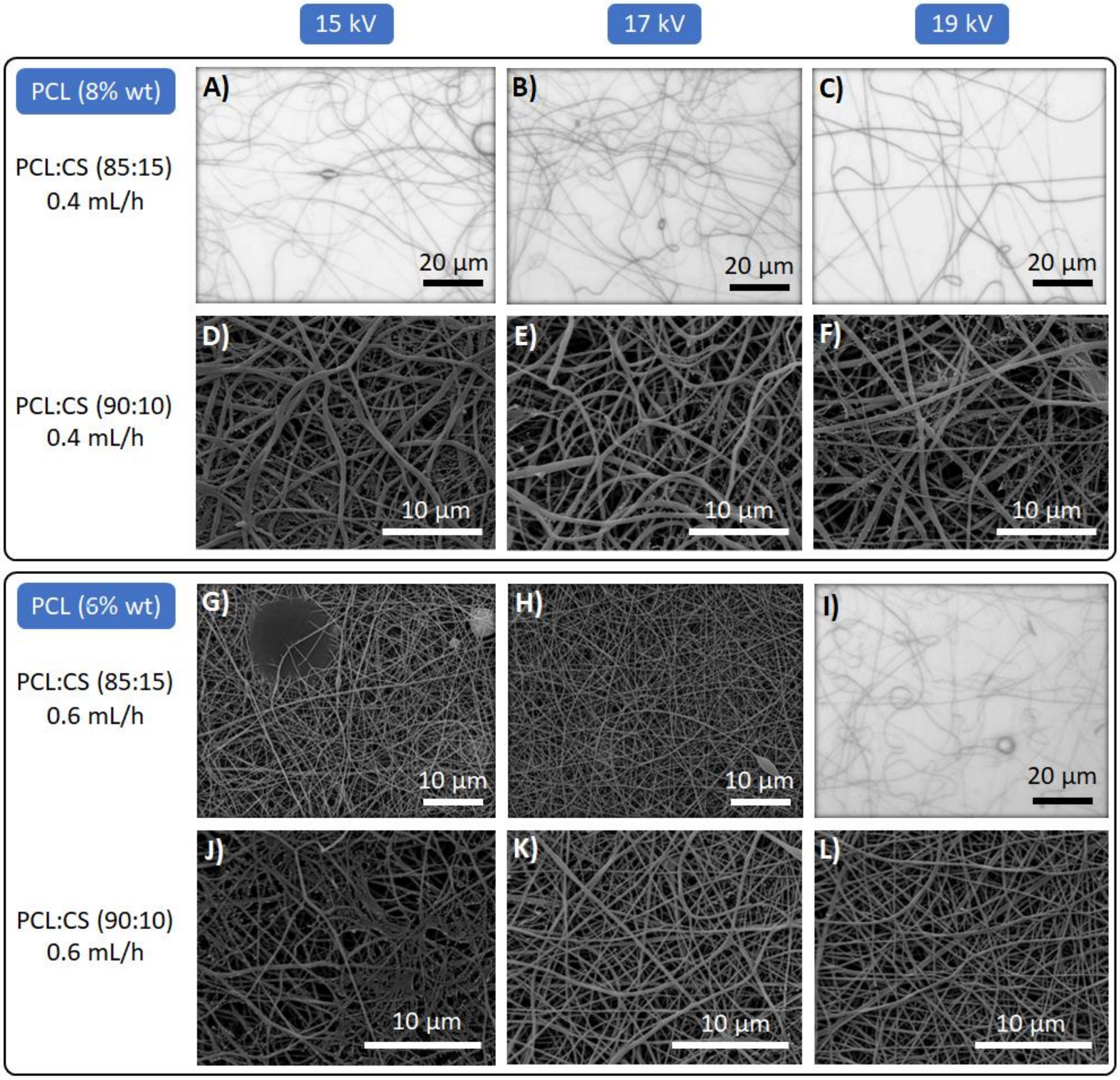

Figure 10. Images of the PCL-CS NFs obtained under different conditions mentioned in Figure 9. A-C e I) optical microscope images of the electrospun fibers directly on a slide since it was not possible to obtain a mat, i.e., very poor electrospinnability at these conditions (red). D-H and J-L) SEM micrographs of the obtained mats.

In addition, the effect of CS on the electrospinning process was evident. With a higher amount of CS, the stability of the jet drops drastically, probably because of polarizable groups in the CS that increase the charge density. Figure 10g-l shows some examples of the NFs obtained with these conditions. In this sense, the instrumental conditions for which the best results were obtained at 19 kV, 12.5 cm collector-needle distance and a flow rate of 0.6 mL/h of the polymer solution. Whereas with the solution at 6 %wt of PCL and a PCL:CS ratio of 90:10 it was possible to obtain a jet of the solution sufficiently constant to obtain the NFs with the required attributes.

Figure 11 shows SEM micrographs and the respective fiber diameter distribution for electrospun mats of PCL, PCL-CS, PCL-CS-P25, PCL-CS-TiO_2TX. In the case of neat PCL, relatively homogeneous and free-beads NFs were obtained with an average diameter of 190 ± 50 nm. For all PCL-CS blends, ultrafine fibers ($d \leq 40$ nm) appeared in a web form between the main fibers. This phenomenon is attributed to the presence of CS [12]. The decrease in fiber diameter was mainly due to the increased charge density in the jet, which imposes higher elongation forces leading to thinner fibers, as described in the literature [34]. In addition, an apparent decrease in the fiber diameters in the blends was observed concerning neat PCL NFs.

In contrast to the smooth and homogeneous surface of PCL-CS NFs, as a result of dispersed NPs on the polymers, PCL-CS-TiO_2 NFs presented a surface with aggregates in diverse zones on the NF. The mean diameters of principal fibers were 160±70 nm and 140±40 nm for PCL-CS-P25 and PCL-CS-TiO_2Tx, respectively. PCL-CS-P25 NFs have a larger mean diameter than PCL-CS-TiO_2Tx due to the presence of remanent surfactant Triton X-100, which also increases the net charge density in the electrospinning jet [69].

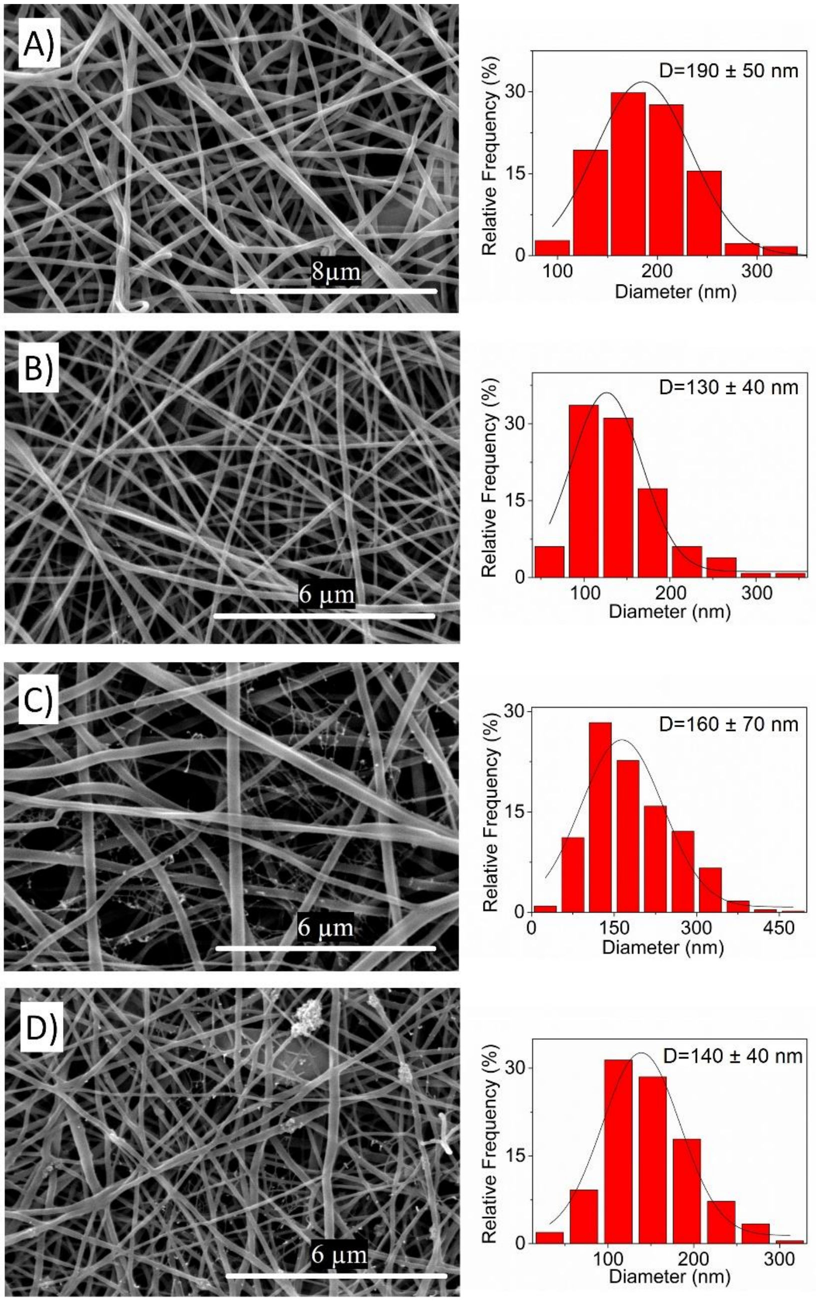

Figure 11. SEM micrographs and corresponding fiber diameter distribution of electrospun mats. A) PCL, B)PCL-CS, C) PCL-CS-P25, D) PCL-CS-TiO_2TX

Figure 12 shows TEM micrographs for PCL-CS-P25 and PCL-CS-TiO_2TX NFs that were electrospun on the copper grid. In both cases, the presence of TiO_2NPs can be observed in the form of small aggregates on the NF surface, whit particles of 20 to 40 nm.

The chemical composition of the electrospun mats was studied by FTIR spectroscopy. Figure 13 shows FTIR spectra of PCL, PCL- CS, PCL-CS-P25, and PCL-CS-TiO_2TX NFs, as well as the spectrum of a CS film for comparative purposes. The PCL absorption bands were located at 2945 and 2865 cm^{-1} attributed to the asymmetric and symmetric stretching vibration of CH_2, respectively; at 1726 cm^{-1} for CO stretching of the ester group; at 1240 and 1175 cm^{-1} for the asymmetric and symmetric stretching vibrations of C-O-C [30]. In the spectra of CS-containing NFs, its characteristic bands with a lower absorbance were observed. A band near 3441 cm^{-1} was assigned to the stretching vibration of the NH and OH groups and at 1545 and 1630 cm^{-1} for the amine and amide groups of CS. Despite its low intensity in this zone, a clear absorbance difference can be observed in the spectra concerning neat PCL NFs, as reported in similar systems [70, 71]. A significant increase in absorbance is also observed in the range of 400 to 700 cm^{-1} which corresponds to the characteristic band of TiO_2 [72]. There is no drastic change in the PCL bands which could indicate that there is no chemical interaction between PCL and NPs. Due to the low absorbance of the CS signals it was not possible to observe the interaction of CS with NPs.

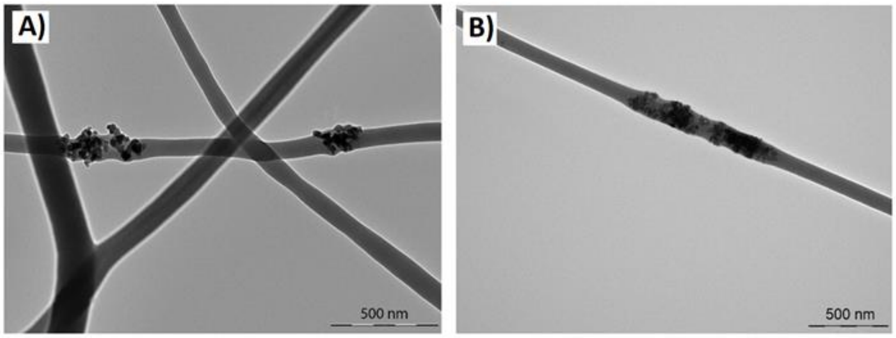

Figure 12. TEM micrographs of the electrospun mats. A) PCL-CS-P25, B) PCL-CS-TiO_2TX

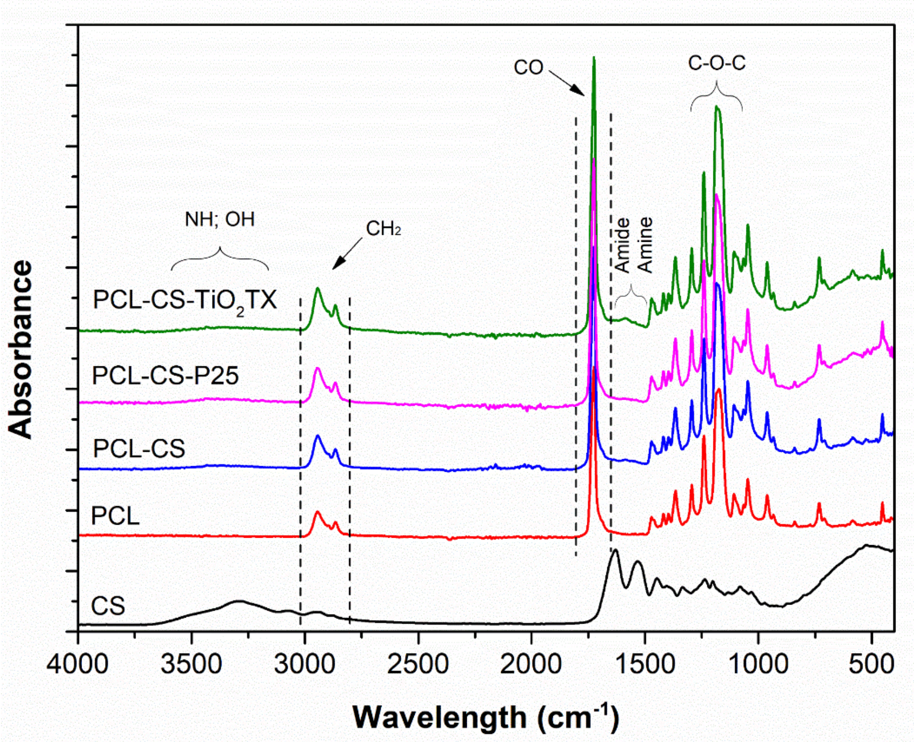

Figure 13. FT-IR spectra of PCL, PCL-CS, PCL-CS-P25, PCL-CS-TiO$_2$TX electrospun mats and CS film.

The thermal degradation profiles obtained by thermogravimetric analysis (TGA) of CS film and PCL, PCL-CS, PCL-CS-NPs NFs (with synthesized and commercial TiO$_2$NPs) are shown in Figure 14 and the data obtained from these are summarized in Table 2. The first weight loss is observed in the range of 50 to 120 °C due to evaporation of water corresponding to sample moisture, with a higher loss for CS film. All PCL-CS-based fibers presented other two main regions of weight loss associated with CS and PCL degradation near 280 and 400 °C, respectively.

As reported, the first weight loss corresponds to the thermal degradation of CS [73]. This process involves the release of H_2O, NH_3, CO, CO_2, and CH_3COOH in the 200-340 °C range [73], after this, the CH_4 generation takes place, and finally, a carbonaceous residue is formed. The thermal degradation profile of PCL shows a significant weight loss near 400 °C, which according to the literature, implies a double simultaneous mechanism, random chain scission and specific chain end scission [74, 75]. The random chain scission is carried out by an intramolecular elimination mechanism (sin Ei) involving the ester group and the β-hydrogen (alkyl group) in a six-membered cyclic transition state [74]. This first degradation step generates H_2O, CO_2 and carboxylic acid as products [74]. At slightly higher temperatures, the specific chain end leads to the formation of ε-caprolactone by depolymerization through an opening mechanism [74]. It is worth noting that no considerable change in the degradation temperature of the materials was observed upon the addition of TiO_2NPs to NFs, most likely due to the small portion of NPs in the material.

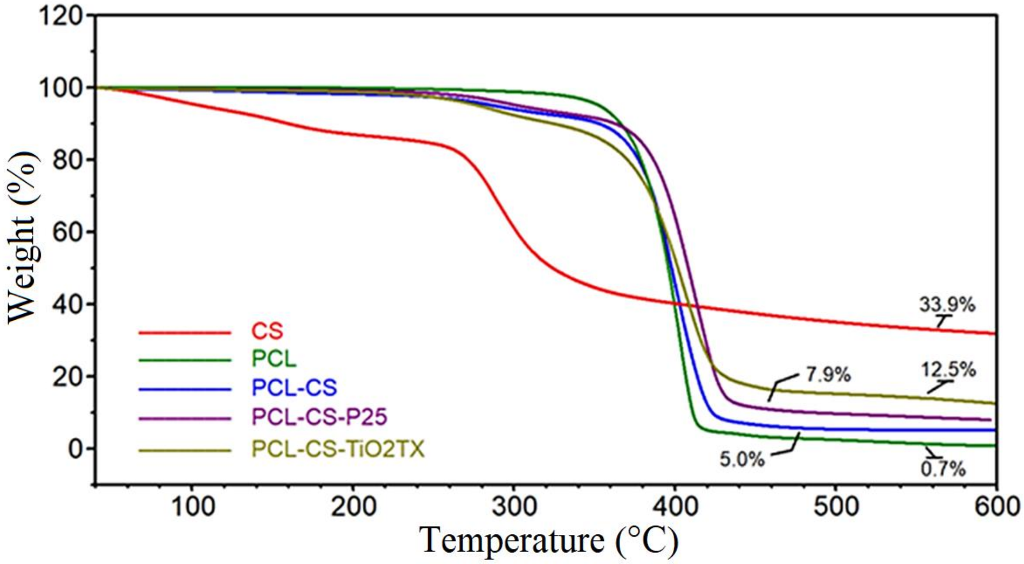

Figure 14. Representative thermal degradation profiles of PCL, PCL-CS, PCL-CS-P25, PCL-CS-TiO_2TX electrospun mats and CS film.

The residual weight percentages after thermal degradation of the polymeric matrix were used to determine the TiO_2NPs amount in the samples, according to Equation 1 [76]. However, it is necessary to evaluate the thermograms excluding the initial water loss stage and the carbonaceous residue remaining at the end. The residual weight at 600 °C was taken to calculate the composition of the mixtures, as no appreciable weight loss was observed above 500 °C. The results obtained are summarized in

Table 3. The actual PCL-CS ratio was determined as 91:9 by weight, while the TiO_2NPs contents in the mats were 4 ± 2 and 5 ± 2 % of commercially available and laboratory synthesized NPs, respectively.

Table 2. Weight decrease (%) of the mats in thermal degradation process.

SAMPLE	25-120 °C (%)	120-335 °C (%)	335-600 °C (%)	RESIDUE (%)
CS	6.3	5.2	54.6	33.9
PCL	0.0	---	99.3*	0.7
PCL-CS	1.0	7.3	86.7	5.0
PCL-CS-P25	0.6	6.8	84.7	7.9
PCL-CS-TIO_2TX	0.7	10.5	76.4	12.5

* Weight decreases in the range of 120-650 °C.

Table 3. Composition of the electrospun mats according to data obtained by thermogravimetric análisis.

MAT	CS (%)	PCL (%)	TiO_2NPs (%)
PCL-CS	9 ± 4	91 ± 5	--
PCL-CS-P25	8 ± 4	88 ± 4	4 ± 2
PCL-CS-TIO_2TX	8 ± 4	87 ± 4	5 ± 2

The thermograms obtained by differential scanning calorimetry (DSC) for NFs mats are shown in Figure 15. All the mats containing PCL exhibited a sharp endothermic signal between the range of 55.7 - 57.0 °C, while this was not observed for the chitosan film [77]. It should be noted that PCL is a semi-crystalline polymer, so it presents amorphous and crystalline phases; the amorphous phase provides the elastomeric properties while the crystalline phase provides the dimensional stability and order to the molecular arrangement of the PCL structure, the latter being responsible for the melting peak shown in the thermograms.

It has been reported that arrangements of amorphous and crystalline phases as well as the degree of crystallinity, are strongly influenced by the electrospinning process [77]. The degree of crystallinity of PCL in NFs (χ_c) was calculated using the following equation:

$$\chi_c = \left(\frac{\Delta H_m}{\Delta H_m^0 x \left(\frac{\% w_{PCL}}{100} \right)} \right) x100$$

Equation 3

Where ΔH_m is the melting enthalpy of PCL in the NFs, ΔH_m^0 is the melting enthalpy of 100 % crystalline PCL, which was considered 142.0 Jg^{-1} [77].%w is the weight percent PCL in the sample, which TGA obtained.

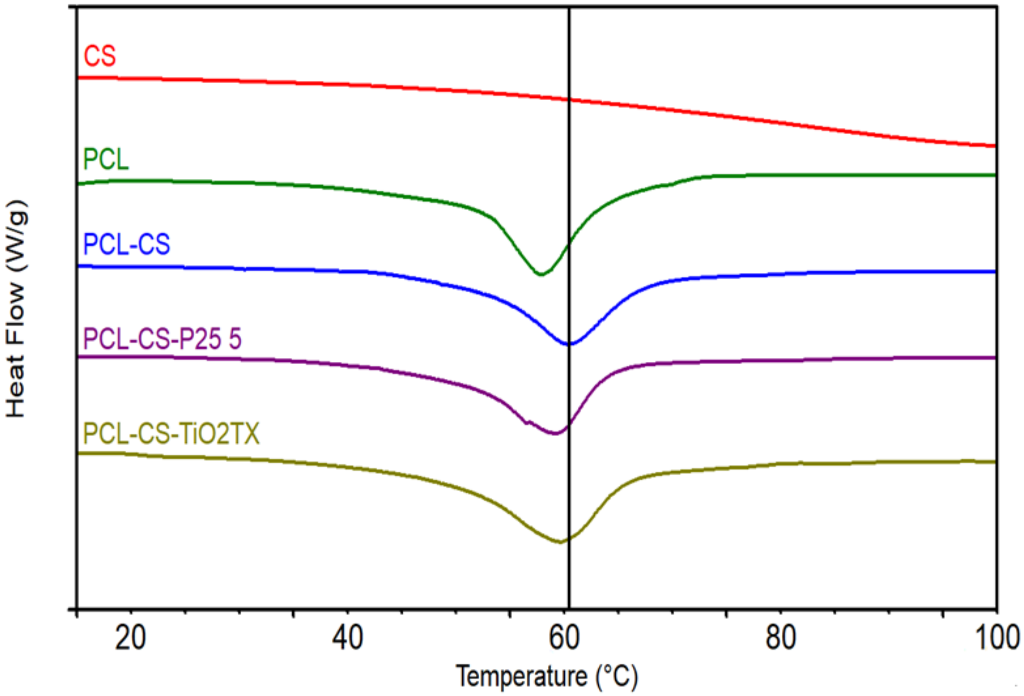

Figure 15. DSC thermograms of the first scan for electrospun mats of PCL, PCL-CS, PCL-CS-P25, PCL-CS-TiO_2TX, and CS film.

Table 4 summarizes the PCL crystallinity percentage (χ_c) obtained to three different heating scans. The first heating scan corresponds to the material obtained directly from the electrospinning process, the second after the heating cycle and a controlled cooling (-10 °C/min), and the last after the previous cycles and a rapid cooling (-50 °C/min). From the χ_c values, it can be inferred that the spinning process favors the crystalline conformation of PCL with considerably higher χ_c values, while when the thermal history of the polymer is eliminated, the crystalline phase is reduced. The same was observed when the material was cooled rapidly, obtaining slightly lower χ_c values due to insufficient time for the organization of the polymer chains [77]. It should be noted that the highest χ_c values were obtained for the mats containing TiO_2NPs, which according to the literature, could indicate a relatively good distribution in the material [78].

Table 4. Melting enthalpy of PCL in the different electrospun mats and the corresponding crystallinity degree.

	CYCLE 1		CYCLE 2		CYCLE 3		χ_c(%)		
	T_m (°C)	**ΔH_m (J/g)**	**T_m (°C)**	**ΔH_m (J/g)**	**T_m (°C)**	**ΔH_m (J/g)**	**1**	**2**	**3**
PCL	58	85.9	56	61.6	55	59.4	60.5	43.4	41.8
PCL-CS	60	71.2	57	56.9	56	55.3	57.7	46.0	44.8
PCL-CS-P25	59	74.2	56	49.5	56	47.2	62.2	41.5	39.5
PCL-CS-TiO_2TX	60	86.7	57	51.3	57	48.4	76.3	45.1	42.6

The effect of TiO_2NPs on the mechanical properties of NFs was studied based on stress-strain curves. A representative example of the measurements performed for each material, PCL-CS, PCL-CS-P25 and PCL-CS-TiO_2TX, is shown in Figure 16. Table 5 summarizes the values extracted from the stress-strain curves for ultimate stress (σ_b), elongation at break (ε_b) and Young's modulus (E), with their respective standard deviation. It was observed that the tensile properties of PCL-CS NFs were slightly improved by adding the TiO_2NPs, increasing the σ_b from 66 to 85 MPa. However, no significant difference was observed in Young's modulus and elongation at break, presenting values of about 400 MPa and 70%, respectively. These results show that adding TiO_2NPs does not negatively affect the electrospun material and can even slightly improve its mechanical properties.

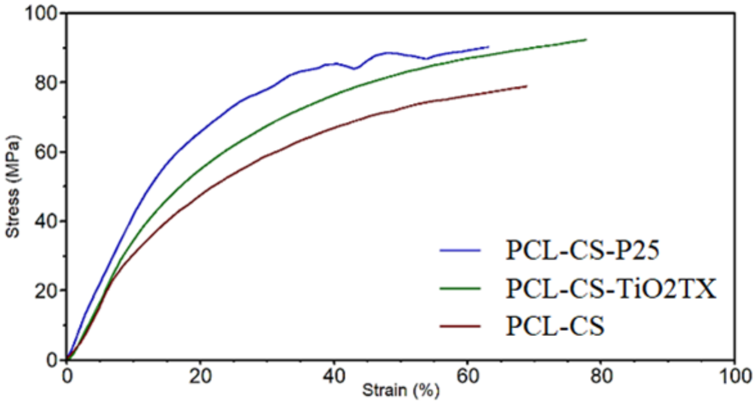

Figure 16. Representative stress-strain curves for PCL-CS, PCL-CS-P25 and PCL-CS-TiO_2TX electrospun mats

Table 5. Mechanical properties and contact angle of PCL-CS, PCL-CS-P25 and PCL-CS-TiO_2TX electrospun mats

Muestra	E (MPa)	ε_b(%)	σ_b (MPa)	Contact angle (°)*
PCL-CS	380 ± 90	75 ± 8	66 ± 8	82 ± 6
PCL-CS-P25	390 ± 90	65 ± 10	90 ± 10	90 ± 10
PCL-CS-TIO_2TX	410 ± 20	80 ± 20	90 ± 10	n.d

*of water on NFs

Continuing with the characterization of the electrospun NFs, the surface wettability of the electrospun mats was evaluated by measuring the contact angle of water droplets on the sample surfaces. The water contact angle values determined for the PCL-CS, PCL-CS-TiO_2TX and PCL-CS-P25 NFs mats are summarized in Table 5.

An overall reduction of the water droplet contact angle on the electrospun membranes compared to neat PCL NFs surfaces (PCL NFs: 188 ± 5° [79]) was obtained, mainly due to the presence of CS in the NFs, which increases the polar contribution in the material [80].

A clear difference was also observed with the addition of both laboratory-synthesized and commercial TiO_2NPs. The mat with commercial TiO_2NPs (P25) showed a slight increase in the contact angle versus the PCL-CS mat without NPs. In contrast, the mat with laboratory-synthesized TiO_2NPs presented a drastic increase in hydrophilicity, resulting in total droplet adsorption in 5-10 s, which prevented reliable measurement of the contact angle. The increase of hydrophilicity se in PCL matrices by adding TiO_2NPs is mainly due to the increase of polar groups on the surface, which generates a more significant interaction between the mat and the solvent liquid [81]. In particular, the significant hydrophilicity increasing of NFs with laboratory synthesized TiO_2NPs can be attributed to Triton X which favors water spreading on surfaces [82].

To know the porosity and pore distribution, the N_2 adsorption-desorption technique was used. N_2 adsorption-desorption isotherms for the BET analysis and Barrett-Joyner-Halenda (BJH) pore size distribution are shown in Figure 17. According to the IUPAC classification, in all cases, a type II isotherm is observed with a hysteresis loop at high relative pressure, characteristic of a material with a wide range of mesopore sizes extending into the macropore range [83]. It should be noted that it presents a type H3 hysteresis, which means it does not exhibit limited adsorption at high relative pressure [84].

BJH pore size distribution plots (Figure 17, D-F) show that the pore distribution is quite heterogeneous, as expected from a material composed of intertwined NFs. It can be observed how there is several pores in the mesoporous range (2-50 nm) and a lower amount in the near macroporous range (>50 nm). However, it should be noted that most of the pores should be in the macroporous range according to the H3 type hysteresis obtained, only that the equipment is not able to discriminate up to this pore diameter (>100 nm).

Table 6 summarizes the specific surface area for the electrospun mats. The PCL mat presented the lowest specific surface area, followed by PCL-CS and finally PCL-CS-P25, the latter presenting the highest total pore volume. This means that the NF-NP hybrid material presents a larger area to interact with the medium, which may favor photocatalytic reactions. These results

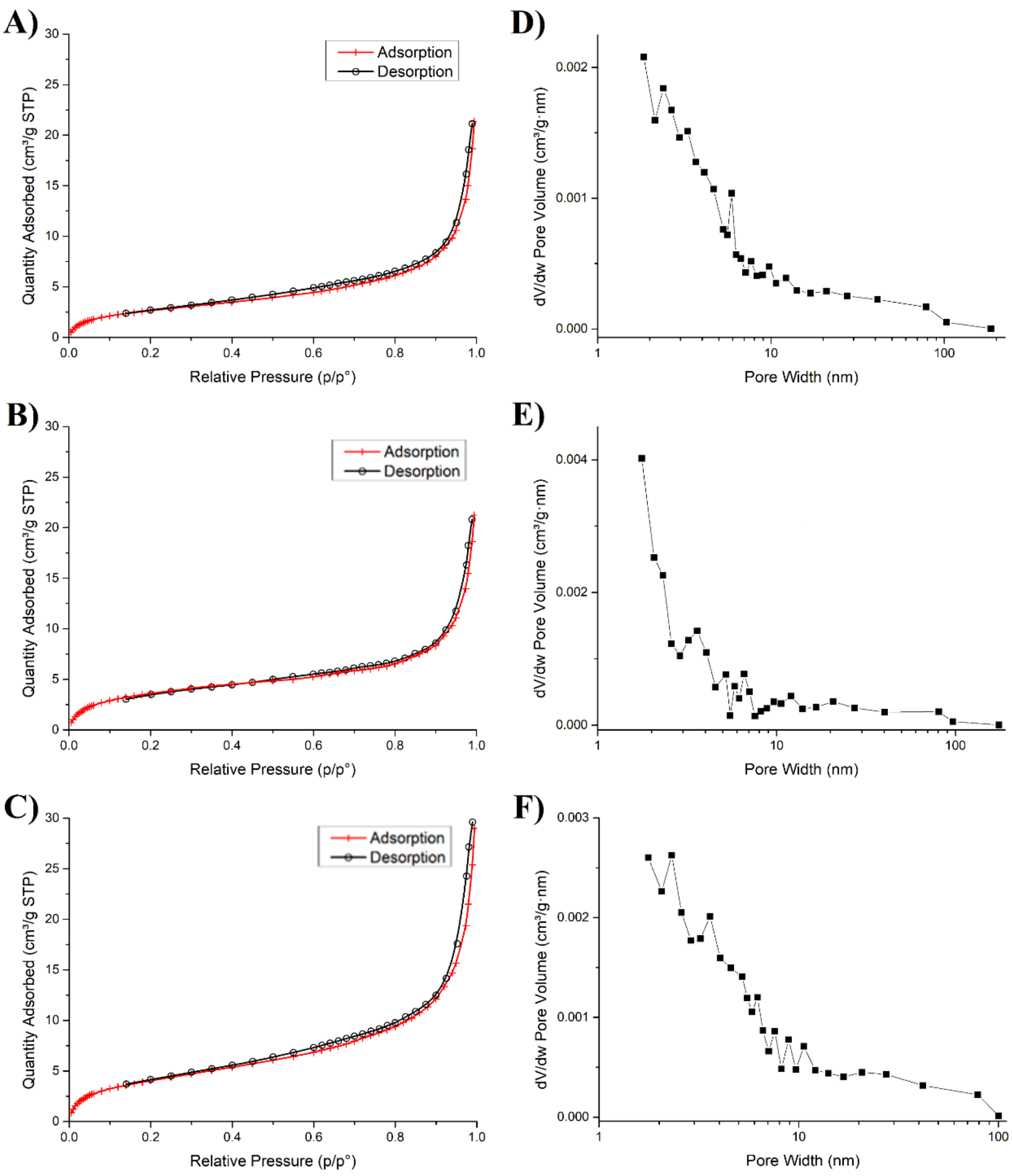

Figure 17. (A-B) N_2 adsorption-desorption isotherms and y (D-F) pore size distribution curves for the NFs of (A,D) PCL, (B,E) PCL-CS y (C,F) PCL-CS-P25.

correspond to the fiber diameters found with the TEM images, following the trend that the smaller the fiber diameter, the larger the surface area.

Table 6. Specific surface area and total pore volume for electrospun mats obtained from N_2 adsorption-desorption isotherms.

Mat	Specific surface BET (m^2/g)	Total pore volume (cm^3/g) $x10^{-2}$
PCL	10.12 ± 0.02	3.27
PCL-CS	13.81 ± 0.07	3.23
PCL-CS-P25	15.28 ± 0.03	4.57

3.3. Study of adsorption properties of electrospun nanofibers.

Adsorption properties of the electrospun NFs were studied through Bach-type experiments by contacting electrospun mats with RhB solution. Figure 18 illustrates the adsorption capacity of PCL, PCL-P25, PCL-CS and PCL-CS-P25 mats with respect to contact time with the RhB solution. It can be observed that for PCL and PCL-P25 NFs no appreciable contaminant adsorption is obtained, having maximum adsorption of around 0.13 mg RhB per gram of mat after 30 hours. While for PCL-CS and PCL-CS-P25, the adsorption curves suggest that the dye binding to active sites had a significant increase up to 90 min and

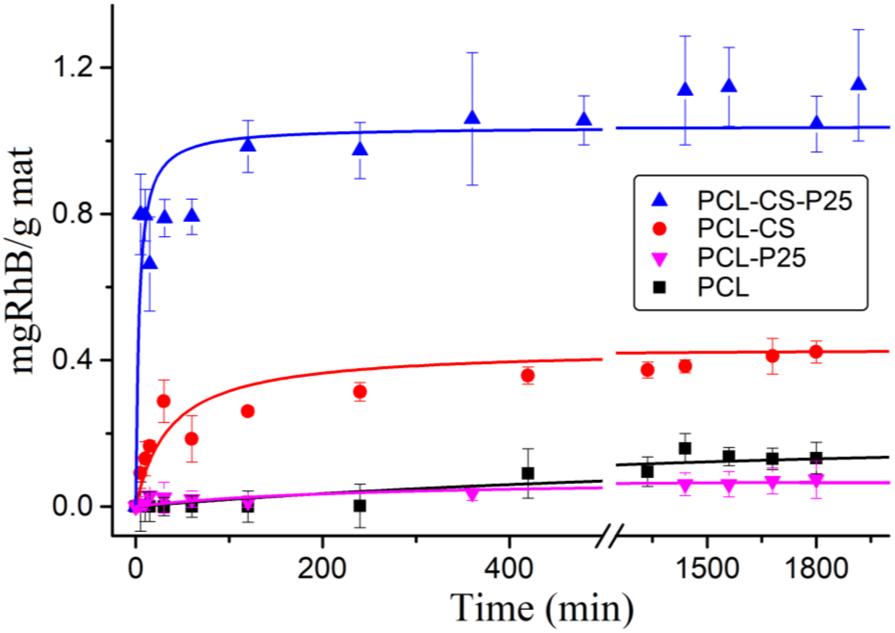

Figure 18. Effect of contact time on the adsorption capacity of RhB, for PCL, PCL-CS, PCL-P25 y PCL-CS-P25.

stabilized around 180 min (3 hours), with maximum adsorption of around 0.42 and 1.15 mg RhB/g mat for PCL-CS and PCL-CS-P25, respectively. In this regard, the adsorption capacity of NFs increased in the order PCL~PCL-P25<PCL-CS<PCL-CS-P25.

Using the surface area obtained by BET, adsorption capacity per unit area was calculated. The adsorption values per unit area is summarized in Table 7, PCL-CS-P25 NFs is the material with the highest amount of RhB adsorbed per gram of mat follow by PCL-CS and PCL. The adsorption values per area values showed that the increase in adsorption was not caused by the increase in the surface area of the NFs but by their composition. The presence of CS in NFs increased the RhB adsorption almost three times, while TiO_2NPs did not show a change in adsorption. Furthermore, when CS and P25 are present at the same time, the adsorption per area of RhB increases to 7.53×10^{-2} mg/m^2 which is not explained by the sum of independent adsorption of each component. Thus, this increase could be attributed to a synergistic effect between them. CS can attract the contaminants to the NFs, i.e. the vicinity of active adsorption sites, such as TiO_2NPs surface and other CS molecules, increasing their maximum capacity. In other words, a bait-hook effect was evidenced. In contrast, PCL-P25 NFs where TiO_2NPs are alone in the NFs, TiO_2NPs do not show this RhB adsorption which means that TiO_2NPs has a lower capacity to attract RhB from the solution bulk.

Table 7. Adsorption of RhB per area of mat

Mat	**Specific surface BET (m^2/g)**	**q_e exp (mg/g)**	**Adsorption per area (mg/m^2) x10^{-2}**
PCL	10.12	0.13	1.28
PCL-CS	13.81	0.42	3.04
PCL-CS-P25	15.28	1.15	7.53

3.3.1. Adsorption kinetics of rhodamine B.

RhB retention can be described as an adsorption process on the polymer surface. Thus, monitoring the time evolution of the process will allow the kinetic description of the process; for this purpose, adsorption kinetic models and adsorption diffusion models were used.

3.3.1.1. Absorption kinetic models

Two models are usually used in the kinetic study of adsorption: the pseudo-first order model (Equation 4) and the pseudo-second order model (Equation 5).
The pseudo-first-order model considers that the adsorption rate is related to the unoccupied active adsorption sites and only one adsorbate can adsorb on an adsorption site on the adsorbent surface. While the pseudo-second-order model assumes that the adsorption capacity is related to the square of the difference between the number of equilibrium adsorption sites on an adsorbent and that of the occupied sites, i.e., it is proportional to the number of active centers of the adsorbent [85].

$$\frac{dq_t}{dt} = k_1(q_e - q_t) \qquad \text{Equation 4}$$

$$\frac{dq_t}{dt} = k_2(q_e - q_t)^2 \qquad \text{Equation 5}$$

Where q_t and q_e (mg/g) correspond to the amount of dye retained at any time, t, and at equilibrium, respectively, and k_1 and k_2 are the pseudo-first-order and pseudo-second-order rate constants, respectively. Integrating these equations at the boundary conditions of q_t=0 at t=0 and q_t=q_t at t=t, and rearranging, we obtain:

- Pseudo-first-order: $q_t = q_e(1 - e^{-k_1 t})$ Equation 6

Linearization: $\ln(q_e - q_t) = \ln q_e - k_1 t$ Equation 7

- Pseudo-second-order: $q_t = \frac{k_2 {q_e}^2 t}{1 + k_2 q_e t}$ Equation 8

Linearization: $\frac{t}{q_t} = \frac{1}{k_2 {q_e}^2} + \frac{t}{q_e}$ Equation 9

However, different authors have exposed some errors when using these kinetic models. Among the most recurrent is the choice of the appropriate contact time to perform the analyses [86]. The contact periods are of utmost importance, from the initial contact of the adsorbate with the sorbent to when the adsorption-desorption phenomenon reaches equilibrium.

Initial times play a critical role in making accurate models, the most remarkable change in adsorbate concentration is observed, and the adsorption mechanism that was followed can be clearly differentiated. As time elapses, the amount of adsorbate adsorbed at any time t (q_t) approaches equilibrium (q_e) and, therefore, the graphical representation of the kinetic data will produce a straight line, regardless of the actual kinetics followed by the system [86]. However, care must also be taken to stop the measurements before reaching equilibrium. Sufficient time should be provided where the adsorption-desorption phenomenon reaches equilibrium, which for most porous materials corresponds to around 24 h.

Continuing with errors in the mathematical implementation of kinetic models to experimental data is the use of linearization of the model equations (Equation 7 y 9) [87, 88]. When the linearized function is used, it is required to perform a linear regression of the data that quantitatively evaluates each parameter. This is fundamentally incorrect since the error structure is also transformed, i.e., homoscedasticity is lost (error variance is not constant), and it also violates the basic assumption of linear regression that the independent variable has a negligible error value [88].

Within these errors, it can be highlighted that for the pseudo-first-order model, qe value is chosen manually by observing the experimental data. In this sense, the qe value cannot be lesser than the maximum measured value of q_t, because it is not possible to obtain the logarithm of negative values resulting in the linearized form Equation 7. In addition, the qe value calculated using the pseudo-first-order model is not equal to the chosen experimental qe value, which should indicate the inability of this model to fit the data [86].

On the other hand, Scatchard linearization in the pseudo-second-order equation (Equation 9), where the time variable is on both sides of the equation, should be highlighted. As well as shown by Zhang [87], this may exaggerate the statistical correlations achieved in the system. In addition, as time is multiplied on the ordinate, at early points in the experiment where there is a substantial decrease in adsorbate concentration, the points are concentrated near the origin, while later data where it is multiplied with higher time values, but with lower sorbate concentration changes, will be farther from the origin and will have a greater weight in the linear regression. This generates a correlation coefficient artificially closer to unity, resulting in many sorption reactions being misclassified as pseudo-second-order reactions [87].

In order to avoid the errors mentioned above, in both models, the fit of the data obtained was performed employing a nonlinear fit as advised by Tran and coworkers [86], using the equation and the raw data directly with as little manipulation as possible.

Table 8 summarizes the parameters of pseudo-first-order and pseudo-second-order kinetic models, such as q_e, k_1, k_2 values, and the correlation coefficients R^2 (best correlation closest to 1) and χ^2 (best correlation closest to 0) in addition to presenting the experimental q_e.

Table 8. Parameters of the pseudo-first-order and pseudo-second-order kinetic models of PCL-CS and PCL-CS-P25.

Mat	q_e exp (mg/g)	Pseudo-first order				Pseudo-Second-order			
		q_e (mg/g)	k_1(min^{-1}) x10^{-2}	χ^2 x10^{-3}	R^2	q_e (mg/g)	k_2(g/min mg) x10^{-2}	χ^2 x10^{-3}	R^2
PCL-CS	0.42	0.38±0.02	1.4±0.4	2.90	0.85	0.43±0.02	6±2	1.49	0.92
PCL-CS-P25	1.15	1.29±0.03	5.3±0.8	8.81	0.94	1.04±0.02	28±7	3.62	0.98

R^2 and χ^2 coefficients were used to choose the kinetic model to which data fit best. In both cases, the closest R^2 values to unity correspond to the pseudo-second-order model, which is corroborated most noticeably with the χ^2 values closest to zero.

In addition to the better fit of data, the calculated values of q_e from the pseudo-second-order kinetic model were much closer to the experimental q_e values. All these results suggest that the adsorption of RhB molecules on the surface of NFs follows a pseudo-second-order kinetic model. This means that the rate-limiting step is chemical sorption; moreover, the adsorption rate depends on the adsorption capacity and not on the concentration of RhB [89].

3.3.1.2. Intra-particle diffusion model

Heterogeneous liquid/solid adsorption process generally involves four main stages: transport in the solution phase, film diffusion, intraparticle diffusion and adsorption on the surface site. Transport from solution and adsorption on the surface are fast steps, so the speed rate of the process is controlled by the diffusion in the porous material. Macropores of electrospun mat are large enough that the diffusion phenomena are not hindered by the pore walls, whereas the mesopores have smaller radios that may hinder diffusion through the walls. In this sense, the overall adsorption rate is controlled by the steps that provide the most significant resistance to mass transport [90].

The possibility that intraparticle diffusion resistance affects adsorption was explored using the following intraparticle diffusion model:

$$q_t = k_p t^{1/2} + c \qquad \text{Equation 10}$$

Where kp is the intraparticle diffusion rate constant, and c (intercept) give an idea about the thickness of the boundary layer (film diffusion), i.e., the larger the intercept the greater the boundary layer effect [91, 92].

Plots of qt vs $t^{1/2}$ are shown in Figure 19 for PCL-CS and PCL-CS-P25 mats. The parameters found by this model are summarized in Table 9. It can be observed that the lines found for the NFs present a small deviation from the origin, indicating that intraparticle diffusion is not the only step controlling the velocity [93]. For PCL-CS-P25, the deviation from the origin is more prominent, so the effect of the boundary layer is larger.

Three straight lines were formed in the plot for the PCL-CS case and two straight lines for PCL-CS-P25, suggesting that intraparticle diffusion occurs via three and two stages, respectively. Allen et al. attribute these diffusion parameters to macropore diffusion, transitional pore diffusion, and micropore diffusion, assuming that the structure of a porous adsorbent can be described as a sinuous pore structure [94].

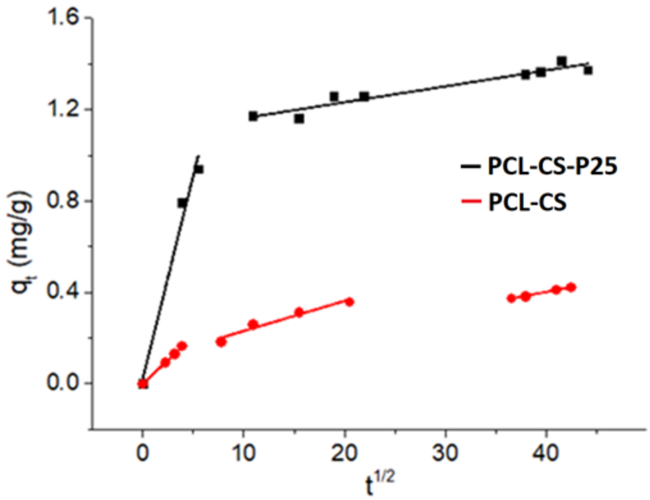

Figure 19. Intraparticle diffusion model plots for PCL-CS and PCL-CS-P25 NFs.

The parameter values $k_{p1} > k_{p2} \approx k_{p3}$, meaning that the diffusion rate of macropores is higher than that of transitional and micropores. This is a direct consequence of the relative free path available for diffusion in each type of pore size. As the adsorbate travels through the material, the pore size decreases, and the "free path" becomes smaller and smaller, which causes a reduction in the diffusion parameters [94]. It should be noted that the values k_{p2} y k_{p3} are very close, and in the case of PCL-CS-P25, only one k_{p2} value is observed; this could be due to a long transitional diffusion stage through the mesopores, due to the wide distribution of mesopore diameters, as discussed above for the nitrogen adsorption-desorption isotherms.

Table 9. Rate constants for intra-particle model

Mat	**Intra-particle model**								
	k_{p1} (mg/ g·min$^{1/2}$)	**c (mg/g)**	**R^2**	**k_{p2} (mg/ g·min$^{1/2}$)**	**c (mg/g)**	**R^2**	**k_{p3} (mg/ g·min$^{1/2}$)**	**c (mg/g)**	**R^2**
PCL-CS	0.042	0.001	0.999	0.0132	0.100	0.930	0.0086	0.060	0.998
PCL-CS-P25	0.178	0.023	0.958	0.0070	1.093	0.914	--		

3.4. Study of photocatalytic activity of electrospun mats under UV irradiation.

In order to evaluate the photoactivity of the fibers, RHB was deposited on the fibers and its degradation was evaluated by fluorecence microscopy under UV irradiation (365 nm). The time-dependent decoloration of RhB under this irradiation is shown in Figure 20, where it can be observed that PCL-CS NFs present a slight decoloration, i.e. low RhB degradation, while PCL-CS-P25 and PCL-CS-TiO_2TX NFs present a much more dramatic photodegradation activity. The above verifies that the photocatalytic properties of TiO_2 are maintained after the electrospinning process.

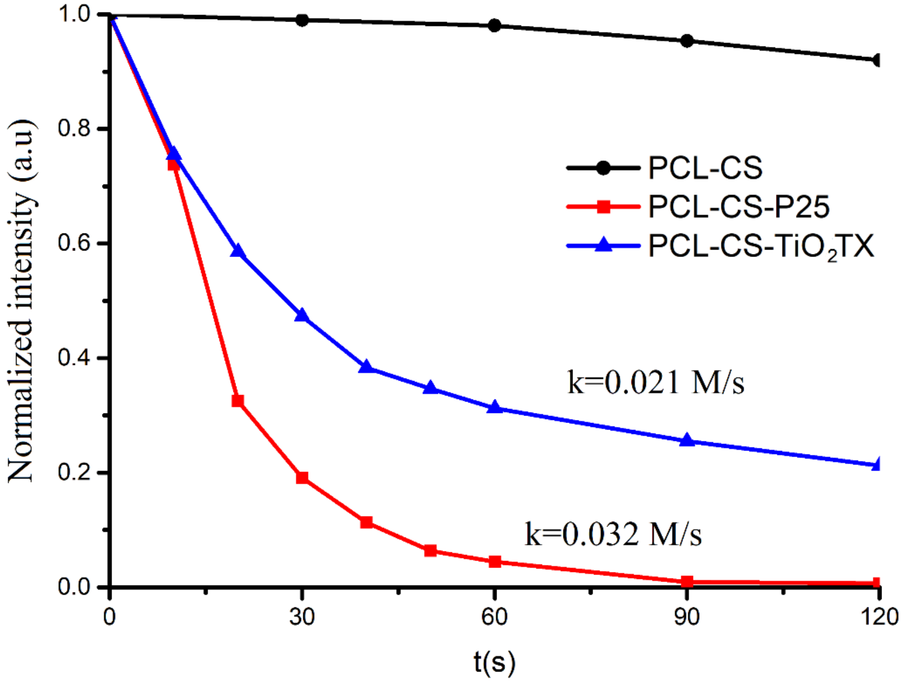

Figure 20. Photocatalytic activity of PCL-CS, PCL-CS-TiO_2TX and PCL-CS-P25 NFs by RhB degradation under UV radiation.

To quantify and compare the photoactivity data of our materials, these were linearly adjusted, obtaining pseudo-zero-order kinetics, whose constants are shown in Figure 20. Pseudo-zero-order kinetics was possibly due to the measurement strategy, where the NFs are saturated with dye, and the excitation radiation directly impacts the material, leading to this kinetic model [95]. PCL-CS-P25 NFs presented a higher rate constant for RhB photodegradation; this could be connected with the fact that P25NPs exhibited better stability in the polymeric solution, in addition to the sensitivity to aggregation presented by the colloidal TiO_2TXNPs due to the pH variation which impairs their activity.

3.5. Study of photocatalytic activity of electrospun mats under visible irradiation in batch-type experiments.

Photocatalytic activity of the electrospun mats was also evaluated by degradation of an RhB aqueous solution using a white LED light (2900-3000 K). These experiments allowed the study of the photocatalysis phenomenon in a system closer to reality and each component's effect on degradation.

In this regard, Figure 21 shows UV-Vis spectra of aqueous solutions of RhB over time for NFs of PCL-CS-P25 and PCL-P25 (in the absence of chitosan). The color of the curves allows visualization of the main effects at each stage of the experiment, from violet curves (t=0 h) through red curves (t=24 h) to blue curves (t=95 or 120 h).

For both systems, RhB solution in the presence of the electrospun materials shows two noticeable changes, one corresponding to a decrease in absorbance and the other to a hypsochromic shift in the maximum absorbance. In the first stage (violet to pink curves), a decrease in the main absorption band at 560 nm is observed, while in the second stage (red to yellow curves), the hypsochromic shift is mainly observed, and in the final stage (blue curves) a prolonged decrease in the absorbance of the band at 498 nm continues. It should be noted that throughout the experiment, both changes occur simultaneously.

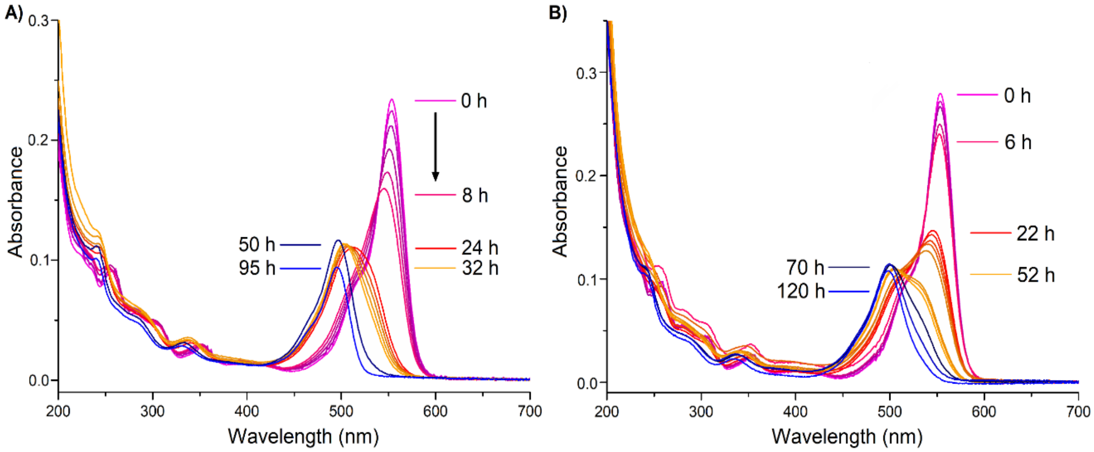

Figure 21. UV-Vis absorption spectra of aqueous solutions of RhB during irradiation. A) PCL-CS-P25; B) PCL-P25.

The loss in absorbance can be attributed to the dye chromophore destruction, and the blue shift is due to N-deethylation of RhB, with the product being rhodamine (λ_{max}=498 nm) [96], (Figure 22, a). This indicates that the degradation pathway proceeded through forming a series of N-deethylated intermediates during the photodegradation reaction process [97]. In addition, a significant change in the reaction rate between rhodamine and RhB is observed, drastically prolonging the reaction times.

Since TiO_2 does not absorb in the visible light range, the semiconductor's role is a little different in this case. Instead of being directly excited by light, the dye absorbs the light and is excited; this electron is transferred to the semiconductor and finally to the electron-accepting substances [98]. In other words, the main character as a dye, its strong visible-light absorption, is exploited to initiate its TiO_2-catalyzed removal. The interaction between the dye and the TiO_2NPs is indispensable for efficiently injecting photoinduced electrons and subsequent degradation reactions. RhB is known to bind to the TiO_2 surface via esterification between the carboxylic group of dye and the hydroxylated TiO_2 surface [98] (See Figure 22,b).

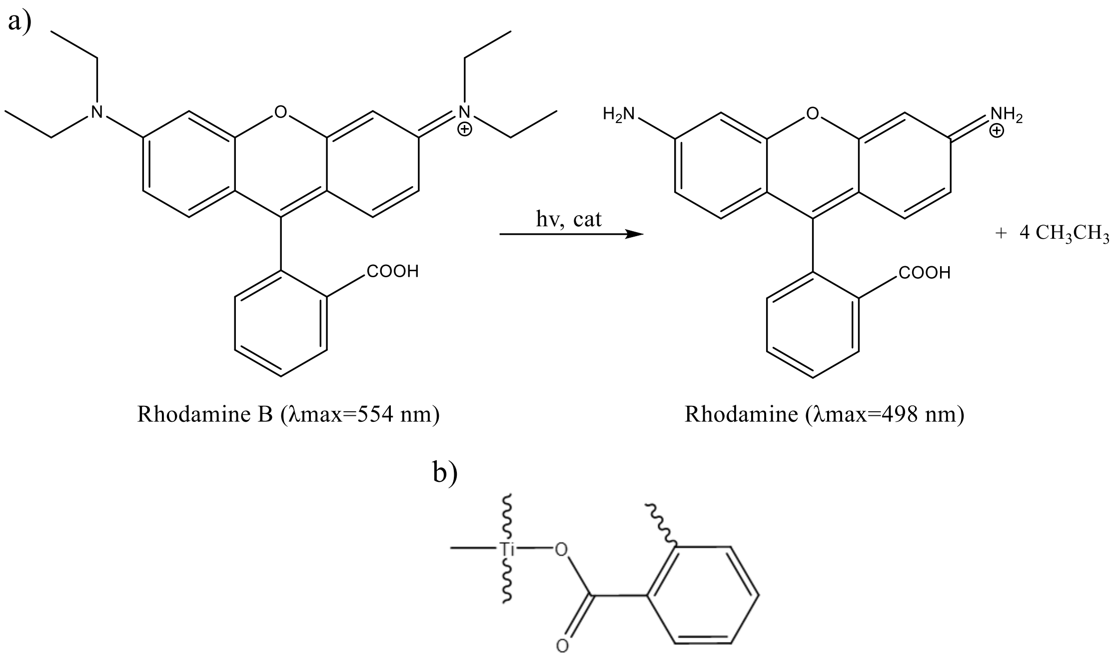

Figure 22. a) N-Deethylation of RhB. b) Interaction between the carboxyl group of RhB and TiO_2 surface [98].

There are two possible routes for electron transfer from the dye to the semiconductor. The first is an injection from the excited state (singlet or triplet) of the dye to the conduction band of TiO_2, and the second, is favored by strong coupling of the π orbital of the dye with the 3d orbital of Ti, which forms a charge transfer complex; thus a charge transfer from ligand to metal (LMCT) occurs, promoting an electron from the basal state of the complex to the conduction band of TiO_2 [98].

Thus, the degradation mechanism would be as follows:

$$RhB + h\nu \rightarrow RhB^* \tag{q}$$

$$RhB^* + TiO_2 \rightarrow RhB^+ + TiO_2(e^-) \tag{r}$$

$$RhB^* + O_2 \rightarrow RhB^+ + {O_2}^- \tag{s}$$

$$TiO_2(e^-) + O_2 \rightarrow TiO_2 + \ {O_2}^- \tag{t}$$

$$RhB^+ \rightarrow rhodamine \rightarrow\rightarrow degradation\, products \tag{u}$$

RhB* can inject electrons into the conduction band of TiO_2, and the cation radical RhB^+ can be formed (equations q and r). RhB^+ can also be formed by electron transfer to oxygen; however, the main route is the r reaction. Oxygen not only acts as the primary electron acceptor in the conduction band (t) but also plays a crucial role in the photochemical N-deethylation process [96].

When the RhB concentration approaches zero, the degradation rate of rhodamine decreases drastically due to the loss of electron injection capacity from an excited state, as the led light used presents an emission minimum at around 500 nm, corresponding to the absorbance maximum of rhodamine.

3.5.1. Degradation kinetics of RhB under visible light in a batch-type experiment.

Figure 23 shows the evolution of RhB concentration as a function of experiment time in the presence of PCL, PCL-CS, PCL-P25, and PCL-CS-P25 NFs.

A solution of RhB was used as a blank, which showed a small decoloration under light irradiation. In the case of the PCL and PCL-CS NFs, a small decrease in the concentration of RhB was observed. However, there was no appreciable differentiation from the blank, i.e., neither PCL nor CS had the capacity to degrade RhB.

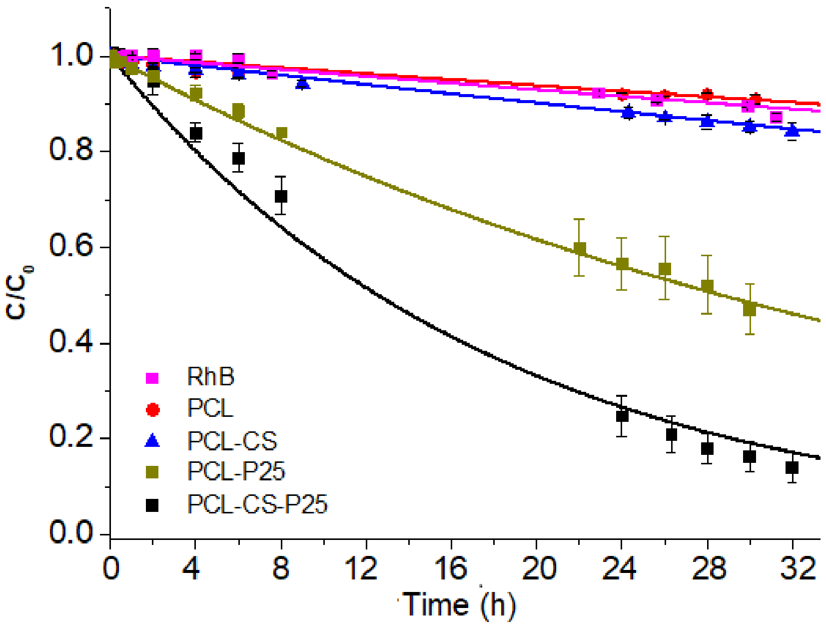

Figure 23. Photocatalytic activity of PCL, PCL-CS, PCL-P25 and PCL-CS-P25 NFs against RhB degradation. Each point represents the mean of three replicates, while the error bars the standard deviation of the mean. A solution of RhB was used as the degradation blank.

The kinetic expression most commonly used to explain heterogeneous catalytic processes is the Langmuir-hinshelwood (LH) kinetic model. In its simplest form, the LH reaction scheme considers a reaction step where the contaminant (C) is reversibly adsorbed on active sites (S) to form an SC adsorption complex. In a second step, the adsorption complex is irreversibly transformed into degraded products and a free active site capable of adsorbing another molecule of contaminant; this process can be schematically described as follows:

$$C + S \underset{k_d}{\overset{k_a}{\rightleftharpoons}} SC \xrightarrow{k_{cat}} P + S$$

Where C is the contaminant, S is the free active site, P is the degraded product, and k_a, k_d, and k_{cat} are the respective adsorption, desorption, and degradation reaction constants rates. The traditional approach to this phenomenon is based on the steady-state approximation for the adsorption complex (SC), which says that the SC concentration does not change on the time scale of product formation [99], resulting in the typical equation of the LH model:

$$r = -\frac{dC}{dt} = \frac{k_{cat}KC}{1+KC} \qquad \text{Equation 11}$$

Where r represents the reaction rate, C is the dye concentration at any time during degradation, and K is the equilibrium constant for the adsorption of the substrate onto the catalyst.

LH kinetics can be reduced to first-order kinetics assuming KC<<<1 [95, 100], resulting in the following equation:

$$-ln\left(\frac{C}{C_0}\right) = k_1 t \qquad \text{Equation 12}$$

Where $k_1=k_{cat}K$.

In other words, the degradation kinetics depend on pollutant concentration, while TiO_2 concentration acts as a constant [101].

As shown in Figure 24, PCL-CS-P25 and PCL-P25 fit the first-order kinetic model very well with R^2 values of 0.998 and 0.983, respectively. Likewise, we also have the corresponding values of k_1 $10.1x10^{-4}$ and $4.4\ x10^{-4}$ min^{-1} for the systems with and without CS, respectively. The rate constant for the NFs with CS is more than double compared to the NFs without CS. Then demonstrates the importance of CS in the decolorization process. As mentioned above, the CS attracts RhB from the bulk solution to the vicinity of the catalysis active

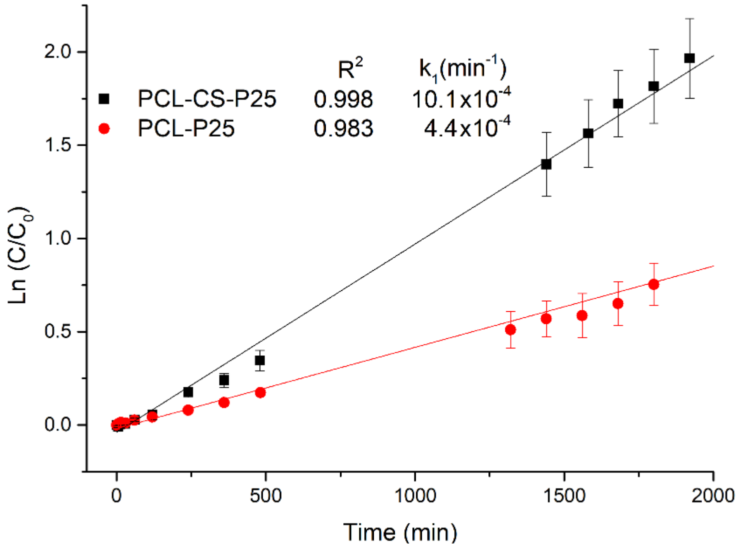

Figure 24. Kinetic curves of RhB photodegradation under visible light.

sites, thus favoring its degradation. In other words, a bait-hook-and-destroy effect was evidenced.

3.6. Effect of the TiO_2NPs amount on the photocatalytic activity.

Figure 25 shows the degradation kinetics of RhB against PCL-CS-P25 NFs with different loading of TiO_2NPs: 5, 10, and 15 wt%. It can be observed that as the amount of catalyst increases, the complete degradation of RhB is achieved faster. The degradation in all cases followed pseudo-first-order kinetics; the values of R^2 and k_1 are summarized in Table 10. As expected, the higher amount of NPs present on the mat, the degradation rate increased. Going from a rate constant of $10.1x10^{-4}$ min^{-1} for 5% loading up to 27.6 $x10^{-4}$ min^{-1} for 15 % TiO_2NPs. The positive impact is because the amount of catalyst is proportional to the number of active OH· and O_2· radicals degrading RhB [102].

Table 10. R^2 and k^1 values of the RhB degradation kinetics by electrospun mats.

Mat	**R^2**	**K_1 (min^{-1}) $x10^{-4}$**
PCL-CS-P25 (5%)	0.998	10.1
PCL-CS-P25 (10%)	0.999	14.6
PCL-CS-P25 (15%)	0.999	27.6

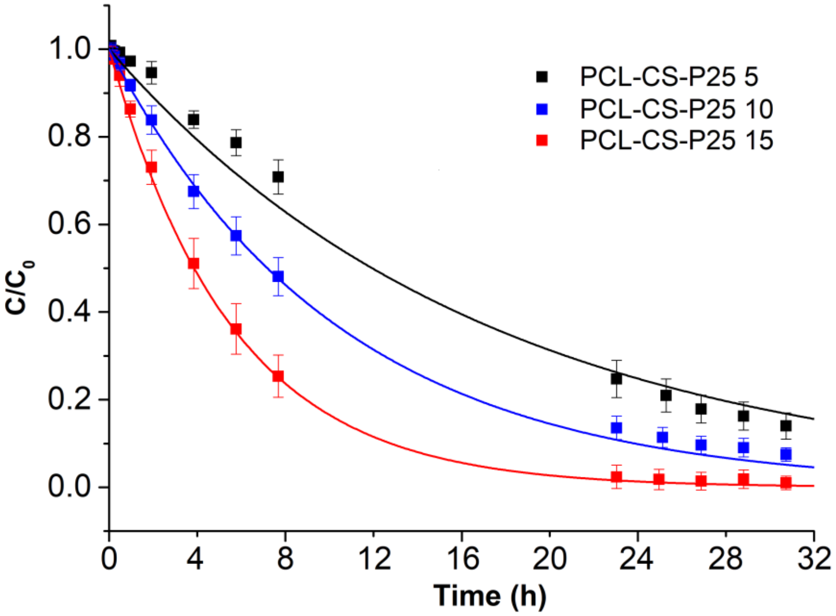

Figure 25. Photocatalytic activity of PCL-CS-P25 NFs with different loading of TiO_2NPs. 5, 10 and 15 wt% TiO_2 NPs on the electrospun mat.

3.7. Use of a sensitizer in the PCL-CS-TiO_2 electrospun matrix.

3.7.1. Characterization of electrospun mats containing PBIJ as a sensitizer.

Figure 26 shows SEM micrographs and the respective fiber diameter distribution for electrospun mats of PCL-CS-PBIJ, PCL-CS-P25-PBIJ, and PCL-CS-TiO_2TX-PBIJ. In all cases, fairly homogeneous and bead-free fibers were obtained, and the presence of ultrafine fibers continued to be observed.

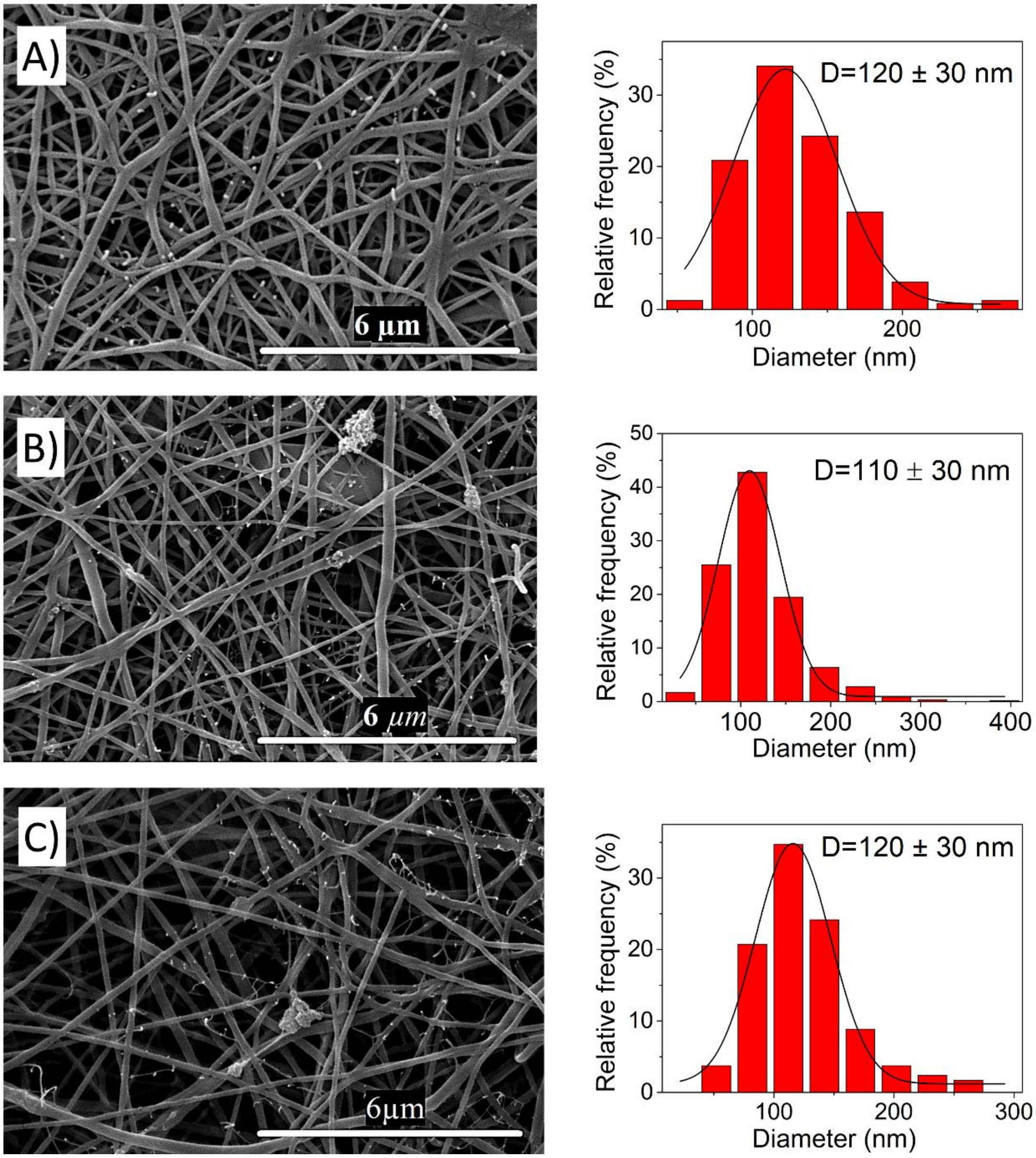

Figure 26. SEM micrographs and corresponding graph of fiber diameter distribution. A) PCL-CS-PBIJ, C) PCL-CS-P25-PBIJ, D) PCL-CS-TiO_2TX-PBIJ.

However, a clear decrease in the stability of the electrospining jet was observed, especially when PCL-CS-TiO_2TX-PBIJ was obtained.

In the case of the PCL-CS-P25-PBIJ and PCL-CS-TiO_2TX-PBIJ mats, small aggregates distributed throughout the material were observed, corresponding to the NPsTiO_2. In the case of PCL-CS-PBIJ, NFs with an average diameter of 120 ± 30 nm were obtained, slightly smaller than PCL-CS without PBIJ. This effect was slightly magnified with the TiO_2NPs addition, obtaining an average diameter of 110 ± 30 and 120 ± 30 nm for PCL-CS-P25-PBIJ and PCL-CS-TiO_2TX-PBIJ NFs, respectively. It is worth noting that comparing the hybridized nanocomposite with and without sensitizer (see Figure 27), the decrease in mean diameters becomes more evident, with a difference of about 50 nm for PCL-CS-P25 and 20 nm for PCL-CS-TiO_2TX. Diameter differences would occur because PBIJ exhibits little surfactant behavior, especially at such low pH [103, 104]. Surfactants decrease surface tension which causes a decreasing in fiber diameter as well as an inherent destabilization of the electrospinning jet and increases the breaking tendency of the extruded filament, with the formation of drops [105, 106].

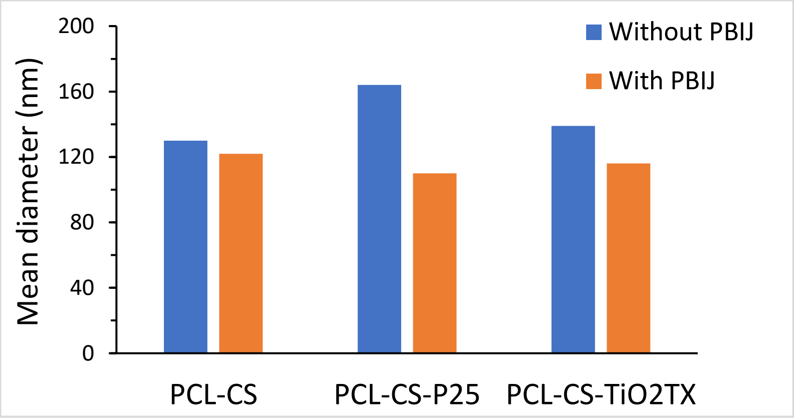

Figure 27. Comparison of mean diameter of electrospun nanofabers with and without PBIJ.

Thermal degradation profiles obtained by TGA of PCL-CS-PBIJ, PCL-CS-P25-PBIJ, PCL-CS-TiO_2TX-PBIJ are shown in Figure 28. Two stages of degradation corresponding to CS and PCL near 280 and 400 °C, respectively, can be determined. The small quantity of sensitizer present in the mats is not sufficient to be determined by this technique since it is impossible to discriminate its degradation stage. However, it was possible to determine the TiO_2 amount from the resulting residues. It was obtained that for both cases was incorporated 6 ± 2 %, very close to its nominal composition of 5 %.

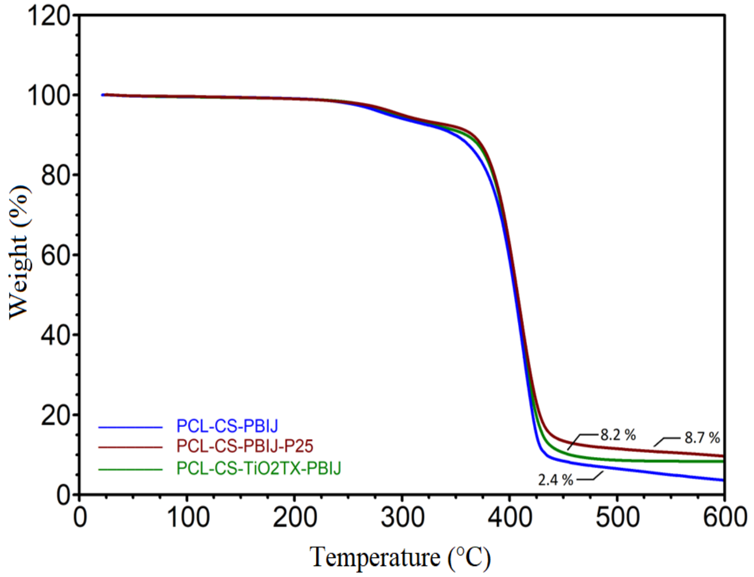

Figure 28. TGA thermal degradation profiles of PCL-CS-PBIJ, PCL-CS-P25-PBIJ, PCL-CS-TiO$_2$TX-PBIJ and PCL-CS-TiO$_2$TX-PBIJ electrospun mats.

Regarding the mechanical properties of mats, Figure 29 shows a representative example of one of the stress vs. strain measurements performed on each mat, PCL-CS-PBIJ, PCL-CS-P25-PBIJ, PCL-CS-TiO$_2$TX-PBIJ. Table 11 summarizes the data extracted from the curves: elongation at break (ε_b), stress at break (σ_b) and Young's modulus (E), each with their respective standard deviation. The tensile properties of PCL-CS NFs were slightly affected by the addition of the sensitizer PBIJ. Young's modulus and ε_b increased, while σ_b decreased compared to the PCL-CS mat. These results mean that the material became slightly harder and tougher, requiring higher strain to achieve lower elongation.

The same was observed in the PCL-CS-P25-PBIJ mat, where E also increased. However, in this case, only stress of 60 ± 10 MPa was necessary to reach 60 ± 20 % elongation, where the rupture occurred. In other words, no higher stress was necessary for the plastic zone of the curve to reach the same elongation at break. Therefore, its plastic behavior is confirmed.

The most significant change in mechanical properties was observed in PCL-CS-TiO$_2$TX-PBIJ mat, where Young's modulus reached a value of 800 ± 80

MPa with an abrupt rupture at an elongation of only 19 ± 5 %. Therefore, it can be said that a brittle plastic material was obtained. This change in tensile properties may be due to the higher amount of surfactant in this material, as it contains the remnant triton X100 from the TiO_2NPs synthesis and Jeffmanin T403 from PBIJ. Surfactants can influence the mechanical properties of electrospun mats [107]. Moreover, as could be observed experimentally, the presence of surfactants in the electrospinning solution increased the instability in the jet, increasing the tendency to breakage of the extruded filament and the increased formation of droplets, directly affecting the tensile properties of the mats [106, 107].

Table 11. Mechanical properties and contact angle of PCL-CS-PBIJ, PCL-CS-P25-PBIJ, PCL-CS-TiO_2TX-PBIJ NFs.

Mat	E (MPa)	ε_b(%)	σ_b (MPa)	Contact angle (°)
PCL-CS-PBIJ	490 ± 50	60 ± 10	80 ± 10	51 ± 3
PCL-CS-P25-PBIJ	470 ± 30	60 ± 20	60 ± 10	50 ± 10
PCL-CS-TIO_2TX-PBIJ	800 ± 80	19 ± 5	90 ± 20	n.d

* Young's modulus (E), elongation at break (ε_b) and strain at break (σ_b)

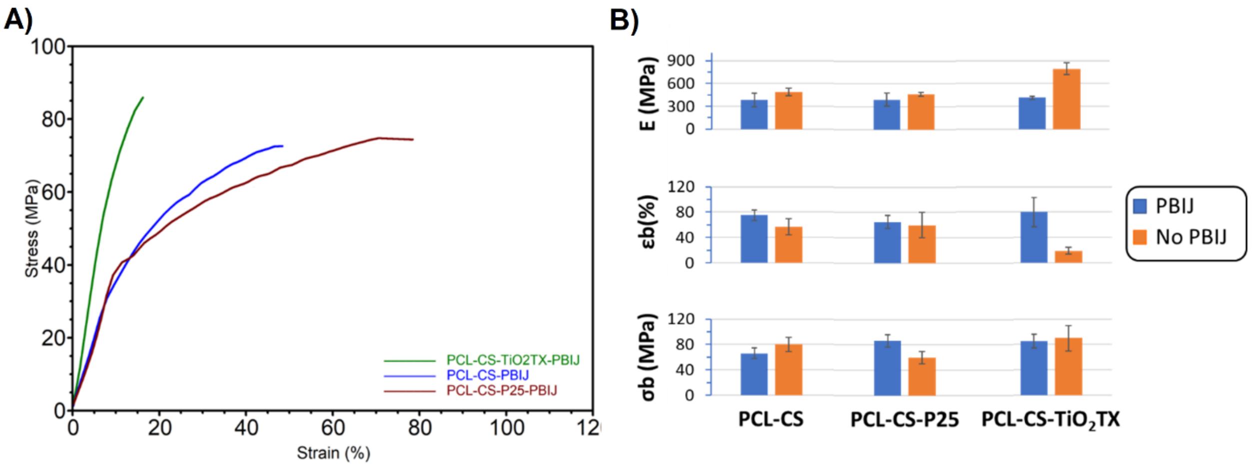

Figure 29. A) Tension-deformation curves and B) Young's modulus (E), elongation at break (ε_b) and strain at break (σ_b) of PCL-CS-PBIJ, PCL-CS-P25-PBIJ, PCL-CS-TiO_2TX-PBIJ NFs.

In this regard, the PCL-CS-TiO_2TX-PBIJ NFs presented a drastic worsening of the tensile properties due to the considerable presence of surfactant, and since no enhanced photocatalytic activity is observed, the material with the commercial TiO_2NPs (P25) is preferred

The values of water droplet contact angle of the PCL-CS-PBIJ, PCL-CS-P25-PBIJ, PCL-CS-TiO_2TX-PBIJ NFs are summarized in Table 11. A significant reduction in contact angle was obtained compared to NFs surfaces without the sensitizer (~90°), which shows an apparent increase in the hydrophilicity of the material. This increment is due to the high number of amino groups and ether groups in the Jeffamine t-403 composing the sensitizer.

3.7.2. Study of the photocatalytic activity of electrospun mats in the presence of a photosensitizer.

Figure 30 shows the photocatalytic activity against UV and visible (blue) radiation in the RhB degradation for PCL-CS, PCL-CS-P25 and PCL-CS-TiO_2TX NFs, where the systems with and without PBIJ are compared. As expected, the PCL-CS system exhibits minimal RhB degradation, which will serve as the target of this study. In the case of UV radiation, the presence of PBIJ very slightly enhanced the photocatalytic activity, as seen in the pseudo-zero order rate constants in Table 12.

Table 12. Pseudo-zero-order kinetic constants of photocatalytic degradation of RhB with the electrospun mats.

Mat	$k_{(UV)}$ ($\times10^{-3}$)	$k_{(Blue)}$ ($\times10^{-3}$)
PCL-CS-P25	-32 ± 2	-0.8 ± 0.1
PCL-CS-P25-PBIJ	-51 ± 9	-19 ± 2
PCL-CS-TiO_2TX	-21 ± 1	-1.8 ± 0.1
PCL-CS-TiO_2TX-PBIJ	-22 ± 1	-3.9 ± 0.3

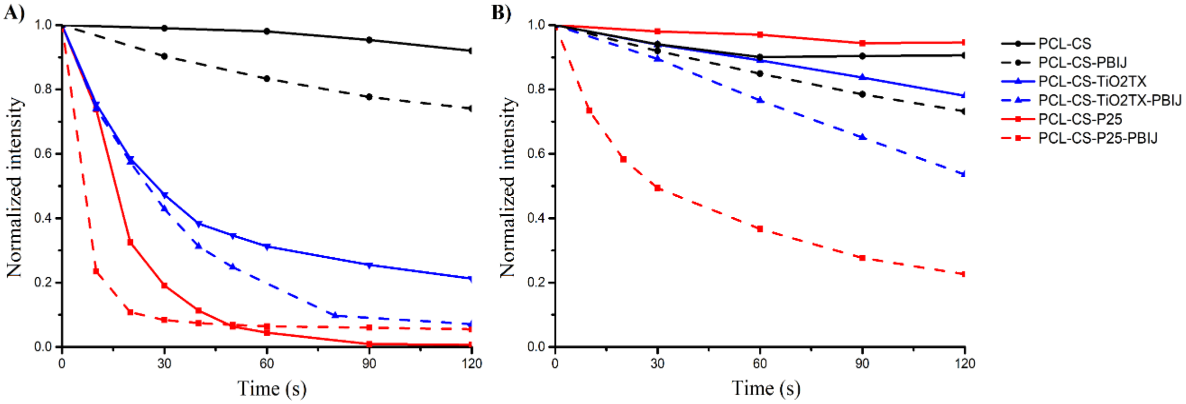

Figure 30. A) Photodegradation kinetics by ultraviolet light irradiation. The addition of PBIJ appeared to slightly increase photoreactivity. B) Photodegradation kinetics using blue light irradiation. The addition of PBIJ caused a dramatic increase in the photoreactivity of the samples.

On the other hand, adding PBIJ to electrospun mats shows dramatic growth in photoactivity under visible light concerning TiO_2 alone. This increment is directly related to the sensitization process of PBIJ to the NPs. As mentioned above, the mechanistic path of degradation is different compared with P25 alone. In this case, PBIJ absorb light irradiation and is excited; this electron is transferred to the semiconductor and finally to the electron-accepting substances [98].

Figure 31, A and B show the PBIJ adsorption emission spectra and TCSPC fluorescence lifetime measurements for PBIJ on the different electrospun mats. As can be seen, quenching in the fluorescence lifetime is obtained in the presence of the NPs, which can be explained by charge transfer from the PBIJ excited state to the TiO_2NPs conduction band. In other words, the fluorescence quenching process shows that PBIJ acts as a sensitizer under visible light irradiation. This sensitization effect is much more dramatic for PCL-CS-P25 going from a rate constant of $0.8x10^{-3}$ to $19x10^{-3}$; this would be due to a good coupling between PBIJ and TiO_2. Thus, the PCL-CS-P25-PBIJ were shown the best material for RhB photodegradation under visible light.

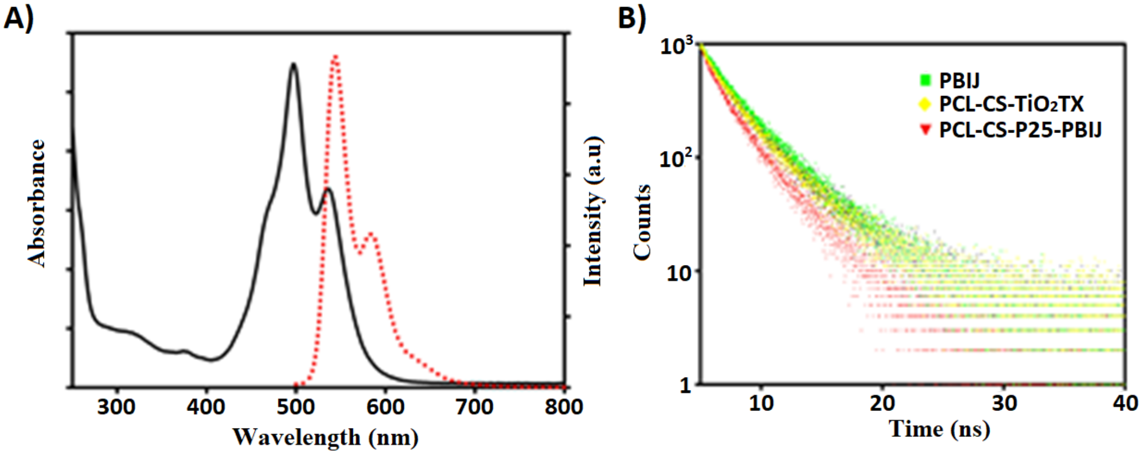

Figure 31. A) Absorption and emission spectra of PBIJ, B) TCSPC fluorescence lifetime measurements for electrospun mats.

In order to have an approach of how this material is positioned compared to others reported in the literature, it should be taken into account that comparison between the reported photocatalytic efficiencies from a unique perspective cannot be achieved due to the different conditions under which the measurements are carried out. Aspects such as, choice of photocatalysis study strategy, light source used, time, initial pollutant concentration, amount of active material, or composition of photocatalyst in the material, etc.; strongly affect the photocatalytic efficiency. The above is reflected in the large amount of information included in Table 13, which summarizes different parameters possible to find in the literature regarding the photocatalytic degradation of RhB using electrospun nanocomposites in the last 5 years.

As shown in the Table 13, PAN and PVDF electrospun fibers have been mostly used in recent years mainly due to its excellent thermal, mechanical stability and high chemical resistance [101, 108-114]. The use of other polymers such as PMMA, PCL and CAB has also been reported [115, 116]. As active components, a great diversity of compounds have been explored, such as $W_{18}O_{49}$ [109], Ag_3PO_4 [111], graphene oxide [112], zin oxide with lanthanides

[114], however the most used is TiO_2 due to low cost, stability in water, and outstanding photocatalytic properties [101, 108, 113]. It should also be noted that the main objective of the research is to favor photocatalytic activity in the visible light spectrum.

To test the photocatalytic activity, lamps with intensity ranging from 100 to 500 w (with filters that select the desired range of light) are normally used, as well as, sunlight simulators and direct solar radiation. Lately the use of LED lights is becoming popular because they have a very narrow wavelength range, the assembly is simpler and the diodes are much more energy and cost efficient. However, their intensity is lower and can cause a drop in photocatalytic activity, but this can be solved by increasing the number of diodes in the system.

As can be seen in the Table 13, the amount of mat, the initial concentration and volume of RhB used in the photocatalytic studies vary considerably. While the mass of mat and the RhB solution concentration/volume used vary between 1 to 200 mg and 10 to 100 mL, respectively. Having an awareness of all these experimental differences from the literature and this work a comparison of the obtained results can be made. The apparent velocity constant (k_1) for the PCL-P25 and PCL-CS-P25 systems under visible radiation is much lower than the other reported systems. However, fluorescence microscopy experiments showed that adding PBIJ to the mat composition improves the initial velocity constant (k_0) by around 23 times, suggesting that the PCL-CS-TiO_2-PBIJ material could reach a degradation rate similar to the systems reported in the literature.

We believe that the main contributions of this work are the following: i) the use of PCL-CS NFs with NPs supported as biomaterials for the remediation of contaminated waters has not been reported before; ii) it is evidenced that it is feasible the election of polymer blends to improve both physical properties and chemical composition of electrospun materials leads to the active action of the polymeric support in the degradation of pollutants generating, for example, a hook effect that attracts the contaminants to the degradation active sites; ii) more environmentally friendly materials are used, e.g. acetic acid-formic acid as solvents instead of more aggressive ones like trifluoroacetic acid and iii) sensitization of photocatalysts by organic dyes as PBIJ considerably improves the photocatalytic activity under visible radiation, allowing the use of low amounts of TiO_2. (≈0.05 g/1 g fiber).

Thus, the current study is expected to contribut to a green and environmentally friendly solution to photocatalysis applications.

Table 13. Photocatalytic parameters reported in studies of the photocatalytic degradation of RhB using electrospun NFs containing different active components, in the last five years.

Polymer	**Active component**	**Rate constant $K_1(h^{-1})$**	**Eff. % (Time,h)**	**Mat (mg)**	**RhB sln Volume/ Concent. (mL/ppm)**	**Light source**	**Ref.**
PAN	TiO_2	1.08	--	50	100 (5)	solar light/ mechanical vibration	[108]
PAN	$W_{18}O_{49}$	--	100% (2h)	--	--(10)	500 W Xenon lamp, visible	[109]
PAN	BiOI-AgI (bismuth oxyiodide-silver iodide)	2.16	100 % (2h)	100	50(10)	150 W Xenon lamp, visible	[110]
PAN	SO_4^{2-}-Ag_3PO_4	3.84	95% (0.8h)	100	50 (10)	200 W Xenon lamp, visible	[111]
PAN-co-MA	Graphene oxide/MIL-101(Fe)/	2.34	100 % (1 h)	4	20(--)	16 W lamp, UV	[112]
PAN/PVDF Core-sheath	TiO_2	--	97% (2 h)	200	30 (10)	300 w lamp, UV	[113]
PVDF	TiO_2	0.25	80 % (6 h)	20	10(10)	White light LED	[101]
PVDF	ZnO:Ln Ln=Sm,La,Er	0.198-0.252	93 % (6 h)	100	100(5)	400 W lamp, visible	[114]
PMMA	$Ag/ZnO/TiO_2$	--	35% (1.5h)	2	10(1)	Sunlight	[115]
CAB	ZnO	--	60 % (8h)	4	10 (4.8)	100 w lamp	[116]
PCL	TiO_2	0.0261	46 % (24h)	3	20 (1)	White light LED	This work
PCL-CS	TiO_2	0.0605	75 % (24h)	3	20 (1)	White light LED	
Fluorescence microscopy							
PCL-CS	TiO_2	K_0=32x10^{-3}	100 % (2min)	~1	10 µL (10)	UV light LED	This work
		K_0=0.8x10^{-3}	5% (2 min)	~1	10 µL (10)	Blue light LED	
		K_0=51x10^{-3}	97% (2min)	~1	10 µL (10)	UV light LED	
PCL-CS	TiO_2-PBIJ	K_0=19x10^{-3}	80 % (2min)	~1	10 µL (10)	Blue light LED	

4. Chapter IV. Conclusions

4.1. Preparation and characterization of the mats

- The experimental parameters that were optimized allowed to obtain homogeneous and bead-free PCL-CS NFs sistems
- Both laboratory-synthesized (TiO_2NPsTX) and commercially purchased (P25) NPs were successfully incorporated ex situ into the polymer matrix. PCL-CS-P25-PBIJ showed better mechanical properties and was therefore preferred for photoactivity tests.
- The adsorption capacity of RhB by the nanocomposites was strongly affected by the composition of the mats. CS considerably favored the adsorption of RhB, and a synergistic effect on it, due to CS and TiO_2NPs simultaneously present in the NFs, was observed.

4.2. Performance in photocatalysis

- A photosensitization of TiO_2 by RhB was evidenced, which caused the degradation of RhB under visible radiation, i.e., species that are able to absorb light and transfer electrons to the catalyst can initiate their degradation on the electrospun material.
- The incorporation of CS in the NFs increased the absorption and degradation of RhB. CS attracted the pollutant molecules to the active sites vicinity of electrospun NFs, favoring initial adsorption and then degradation. In other words, a bait-hook-and-destroy effect was evidenced.
- In the absence of any sensitizer, the RhB degradation occurs more rapidly under UV irradiation, where TiO_2NPs can directly absorb light. PCL-CS-P25 was the material with the highest activity.
- PCL-CS-P25-PBIJ NFs, in addition to better tensile properties, showed better photocatalytic activity in degration of RhB. While, PCL-CS-TiO_2TX-PBIJ presented a lower photocatalytic activity and was a much more rigid

and brittle material. Thus, it was shown how it is possible to modulate the NFs properties by changing the NPs incorporated.

- Sensitization by organic dyes as PBIJ considerably improves the photocatalytic activity under visible radiation, allowing the use of low amounts of TiO_2. (≈0.05 g TiO_2/g of fiber). Thus, the current study is expected to provide an environmentally friendly green solution to photocatalysis applications.

Bibliography

[1] D. B. Miklos, C. Remy, M. Jekel, K. G. Linden, J. E. Drewes, and U. Hübner, "Evaluation of advanced oxidation processes for water and wastewater treatment – A critical review," *Water Research,* vol. 139, pp. 118-131, 2018, doi: 10.1016/j.watres.2018.03.042.

[2] S. T. M *et al.*, "A review of recent progress in polymeric electrospun nanofiber membranes in addressing safe water global issues," *RSC Advances,* vol. 11, no. 16, pp. 9638-9663, 2021, doi: 10.1039/D1RA00060H.

[3] F. Fadil, N. D. Affandi, M. I. Misnon, N. N. Bonnia, A. M. Harun, and M. K. Alam, "Review on Electrospun Nanofiber-Applied Products," *Polymers*, vol. 13, no. 13, doi: 10.3390/polym13132087.

[4] R. Vasita and D. S. Katti, "Nanofibers and their applications in tissue engineering," (in eng), *Int J Nanomedicine,* vol. 1, no. 1, pp. 15-30, 2006, doi: 10.2147/nano.2006.1.1.15.

[5] R. Khajavi, M. Abbasipour, and A. Bahador, "Electrospun biodegradable nanofibers scaffolds for bone tissue engineering," *Journal of Applied Polymer Science,* vol. 133, no. 3, 2016, doi: 10.1002/app.42883.

[6] T. Garg, G. Rath, and A. K. Goyal, "Biomaterials-based nanofiber scaffold: targeted and controlled carrier for cell and drug delivery," *Journal of Drug Targeting,* vol. 23, no. 3, pp. 202-221, 2015, doi: 10.3109/1061186X.2014.992899.

[7] Q. Yang, X. Jiang, F. Gu, Z. Ma, J. Zhang, and L. Tong, "Polymer micro or nanofibers for optical device applications," *Journal of Applied Polymer Science,* vol. 110, no. 2, pp. 1080-1084, 2008, doi: 10.1002/app.28716.

[8] E. Scholten, L. Bromberg, G. C. Rutledge, and T. A. Hatton, "Electrospun Polyurethane Fibers for Absorption of Volatile Organic Compounds from Air," *ACS Applied Materials & Interfaces,* vol. 3, no. 10, pp. 3902-3909, 2011, doi: 10.1021/am200748y.

[9] L. Van der Schueren, I. Steyaert, B. De Schoenmaker, and K. De Clerck, "Polycaprolactone/chitosan blend nanofibres electrospun from an acetic acid/formic acid solvent system," *Carbohydrate Polymers,* vol. 88, no. 4, pp. 1221-1226, 2012, doi: 10.1016/j.carbpol.2012.01.085.

[10] S. Haider and S.-Y. Park, "Preparation of the electrospun chitosan nanofibers and their applications to the adsorption of Cu(II) and Pb(II)

ions from an aqueous solution," *Journal of Membrane Science,* vol. 328, no. 1, pp. 90-96, 2009, doi: 10.1016/j.memsci.2008.11.046.

[11] K. Sun and Z. H. Li, "Preparations, properties and applications of chitosan based nanofibers fabricated by electrospinning," *Express Polym. Lett.,* vol. 5, pp. 342-361, 2011, doi: 10.3144/expresspolymlett.2011.34.

[12] L. Van der Schueren *et al.*, "Polycaprolactone and polycaprolactone/chitosan nanofibres functionalised with the pH-sensitive dye Nitrazine Yellow," *Carbohydrate Polymers,* vol. 91, no. 1, pp. 284-293, 2013, doi: 10.1016/j.carbpol.2012.08.003.

[13] A. Suzuki and Y. Shimba, "Poly(l-lactic acid) twisted nanofiber yarn prepared by carbon dioxide laser supersonic multi-drawing," *European Polymer Journal,* vol. 110, pp. 145-154, 2019, doi: 10.1016/j.eurpolymj.2018.11.028.

[14] Y. Gao *et al.*, "Recent progress and challenges in solution blow spinning," *Materials Horizons,* vol. 8, no. 2, pp. 426-446, 2021, doi: 10.1039/D0MH01096K.

[15] L. Ren and S. P. Kotha, "Centrifugal jet spinning for highly efficient and large-scale fabrication of barium titanate nanofibers," *Materials Letters,* vol. 117, pp. 153-157, 2014, doi: 10.1016/j.matlet.2013.11.103.

[16] X. Xing, Y. Wang, and B. Li, "Nanofiber drawing and nanodevice assembly in poly(trimethylene terephthalate)," *Opt. Express,* vol. 16, no. 14, pp. 10815-10822, 2008, doi: 10.1364/OE.16.010815.

[17] J. Song, M. Kim, and H. Lee, "Recent Advances on Nanofiber Fabrications: Unconventional State-of-the-Art Spinning Techniques," *Polymers,* vol. 12, no. 6, p. 1386, 2020, doi: 10.3390/polym12061386.

[18] Kenry and C. T. Lim, "Nanofiber technology: current status and emerging developments," *Progress in Polymer Science,* vol. 70, pp. 1-17, 2017, doi: 10.1016/j.progpolymsci.2017.03.002.

[19] K. T. Shalumon, K. H. Anulekha, C. M. Girish, R. Prasanth, S. V. Nair, and R. Jayakumar, "Single step electrospinning of chitosan/poly(caprolactone) nanofibers using formic acid/acetone solvent mixture," *Carbohydrate Polymers,* vol. 80, no. 2, pp. 413-419, 2010, doi: 10.1016/j.carbpol.2009.11.039.

[20] R. C. Cheung, T. B. Ng, J. H. Wong, and W. Y. Chan, "Chitosan: An Update on Potential Biomedical and Pharmaceutical Applications," *Marine Drugs*, vol. 13, no. 8, pp. 5156-5186doi: 10.3390/md13085156.

[21] D. Wei, Y. Ye, X. Jia, C. Yuan, and W. Qian, "Chitosan as an active support for assembly of metal nanoparticles and application of the resultant bioconjugates in catalysis," *Carbohydrate Research,* vol. 345, no. 1, pp. 74-81, 2010, doi: 10.1016/j.carres.2009.10.008.

[22] H. Huang, Q. Yuan, and X. Yang, "Preparation and characterization of metal–chitosan nanocomposites," *Colloids and Surfaces B: Biointerfaces,* vol. 39, no. 1, pp. 31-37, 2004, doi: 10.1016/j.colsurfb.2004.08.014.

[23] D. K. Verma, R. Malik, J. Meena, and R. Rameshwari, "Synthesis, characterization and applications of chitosan based metallic nanoparticles: A review," *Journal of Applied and Natural Science,* vol. 13, no. 2, pp. 544 - 551, 2021, doi: 10.31018/jans.v13i2.2635.

[24] M. Ishihara, V. Q. Nguyen, Y. Mori, S. Nakamura, and H. Hattori, "Adsorption of Silver Nanoparticles onto Different Surface Structures of Chitin/Chitosan and Correlations with Antimicrobial Activities," *International Journal of Molecular Sciences*, vol. 16, no. 6, pp. 13973-13988doi: 10.3390/ijms160613973.

[25] K. Ohkawa, D. Cha, H. Kim, A. Nishida, and H. Yamamoto, "Electrospinning of Chitosan," *Macromolecular Rapid Communications,* vol. 25, no. 18, pp. 1600-1605, 2004, doi: 10.1002/marc.200400253.

[26] M. Aliabadi, M. Irani, J. Ismaeili, H. Piri, and M. J. Parnian, "Electrospun nanofiber membrane of PEO/Chitosan for the adsorption of nickel, cadmium, lead and copper ions from aqueous solution," *Chemical Engineering Journal,* vol. 220, pp. 237-243, 2013, doi: 10.1016/j.cej.2013.01.021.

[27] F. Sharifi, S. M. Atyabi, D. Norouzian, M. Zandi, S. Irani, and H. Bakhshi, "Polycaprolactone/carboxymethyl chitosan nanofibrous scaffolds for bone tissue engineering application," *International Journal of Biological Macromolecules,* vol. 115, pp. 243-248, 2018, doi: 10.1016/j.ijbiomac.2018.04.045.

[28] D. Jhala, H. Rather, and R. Vasita, "Polycaprolactone–chitosan nanofibers influence cell morphology to induce early osteogenic differentiation," *Biomaterials Science,* vol. 4, no. 11, pp. 1584-1595, 2016, doi: 10.1039/C6BM00492J.

[29] G. Wu, X. Deng, J. Song, and F. Chen, "Enhanced biological properties of biomimetic apatite fabricated polycaprolactone/chitosan nanofibrous bio-composite for tendon and ligament regeneration," *Journal of Photochemistry and Photobiology B: Biology,* vol. 178, pp. 27-32, 2018, doi: 10.1016/j.jphotobiol.2017.10.011.

[30] N. P. Rijal, U. Adhikari, S. Khanal, D. Pai, J. Sankar, and N. Bhattarai, "Magnesium oxide-poly(ε-caprolactone)-chitosan-based composite nanofiber for tissue engineering applications," *Materials Science and Engineering: B,* vol. 228, pp. 18-27, 2018, doi: 10.1016/j.mseb.2017.11.006.

[31] S. Wang, Y. Li, R. Zhao, T. Jin, L. Zhang, and X. Li, "Chitosan surface modified electrospun poly(ε-caprolactone)/carbon nanotube composite fibers with enhanced mechanical, cell proliferation and antibacterial properties," *International Journal of Biological Macromolecules,* vol. 104, pp. 708-715, 2017, doi: 10.1016/j.ijbiomac.2017.06.044.

[32] S. Gomes, G. Rodrigues, G. Martins, C. Henriques, and J. C. Silva, "Evaluation of nanofibrous scaffolds obtained from blends of chitosan, gelatin and polycaprolactone for skin tissue engineering," *International Journal of Biological Macromolecules,* vol. 102, pp. 1174-1185, 2017, doi: 10.1016/j.ijbiomac.2017.05.004.

[33] K. Kalwar, W.-X. Sun, D.-L. Li, X.-J. Zhang, and D. Shan, "Coaxial electrospinning of polycaprolactone@chitosan: Characterization and silver nanoparticles incorporation for antibacterial activity," *Reactive and Functional Polymers,* vol. 107, pp. 87-92, 2016, doi: 10.1016/j.reactfunctpolym.2016.08.010.

[34] F. M. Ghorbani, B. Kaffashi, P. Shokrollahi, E. Seyedjafari, and A. Ardeshirylajimi, "PCL/chitosan/Zn-doped nHA electrospun nanocomposite scaffold promotes adipose derived stem cells adhesion and proliferation," *Carbohydrate Polymers,* vol. 118, pp. 133-142, 2015, doi: 10.1016/j.carbpol.2014.10.071.

[35] K. Karakas, A. Celebioglu, M. Celebi, T. Uyar, and M. Zahmakiran, "Nickel nanoparticles decorated on electrospun polycaprolactone/chitosan nanofibers as flexible, highly active and reusable nanocatalyst in the reduction of nitrophenols under mild conditions," *Applied Catalysis B: Environmental,* vol. 203, pp. 549-562, 2017, doi: 10.1016/j.apcatb.2016.10.020.

[36] C.-G. Lee *et al.*, "Porous Electrospun Fibers Embedding TiO2 for Adsorption and Photocatalytic Degradation of Water Pollutants,"

Environmental Science & Technology, vol. 52, no. 7, pp. 4285-4293, 2018, doi: 10.1021/acs.est.7b06508.

[37] A. Salama, A. Mohamed, N. M. Aboamera, T. A. Osman, and A. Khattab, "Photocatalytic degradation of organic dyes using composite nanofibers under UV irradiation," *Applied Nanoscience,* vol. 8, no. 1, pp. 155-161, 2018, doi: 10.1007/s13204-018-0660-9.

[38] Z. Guo, R. Ma, and G. Li, "Degradation of phenol by nanomaterial TiO2 in wastewater," *Chemical Engineering Journal,* vol. 119, no. 1, pp. 55-59, 2006, doi: 10.1016/j.cej.2006.01.017.

[39] H. Gu, X. Chen, F. Chen, X. Zhou, and Z. Parsaee, "Ultrasound-assisted biosynthesis of CuO-NPs using brown alga Cystoseira trinodis: Characterization, photocatalytic AOP, DPPH scavenging and antibacterial investigations," *Ultrasonics Sonochemistry,* vol. 41, pp. 109-119, 2018, doi: 10.1016/j.ultsonch.2017.09.006.

[40] C. B. Ong, L. Y. Ng, and A. W. Mohammad, "A review of ZnO nanoparticles as solar photocatalysts: Synthesis, mechanisms and applications," *Renewable and Sustainable Energy Reviews,* vol. 81, pp. 536-551, 2018, doi: 10.1016/j.rser.2017.08.020.

[41] J. Rivera-Utrilla, M. Sánchez-Polo, M. Á. Ferro-García, G. Prados-Joya, and R. Ocampo-Pérez, "Pharmaceuticals as emerging contaminants and their removal from water. A review," *Chemosphere,* vol. 93, no. 7, pp. 1268-1287, 2013, doi: 10.1016/j.chemosphere.2013.07.059.

[42] M. L. Yola, T. Eren, and N. Atar, "A novel efficient photocatalyst based on TiO2 nanoparticles involved boron enrichment waste for photocatalytic degradation of atrazine," *Chemical Engineering Journal,* vol. 250, pp. 288-294, 2014, doi: 10.1016/j.cej.2014.03.116.

[43] Y. Nosaka and A. Y. Nosaka, "Generation and Detection of Reactive Oxygen Species in Photocatalysis," *Chemical Reviews,* vol. 117, no. 17, pp. 11302-11336, 2017, doi: 10.1021/acs.chemrev.7b00161.

[44] Q. I. Rahman, M. Ahmad, S. K. Misra, and M. Lohani, "Effective photocatalytic degradation of rhodamine B dye by ZnO nanoparticles," *Materials Letters,* vol. 91, pp. 170-174, 2013, doi: 10.1016/j.matlet.2012.09.044.

[45] J. Li, W. Ma, C. Chen, J. Zhao, H. Zhu, and X. Gao, "Photodegradation of dye pollutants on one-dimensional TiO2 nanoparticles under UV and visible irradiation," *Journal of Molecular Catalysis A: Chemical,* vol. 261, no. 1, pp. 131-138, 2007, doi: 10.1016/j.molcata.2006.08.018.

[46] M. Y. Nassar, H. M. Aly, M. E. Moustafa, and E. A. Abdelrahman, "Synthesis, Characterization and Biological Activity of New 3-substitued-4-amino-5-hydrazino-1,2,4-triazole Schiff Bases and Their Cu(II) Complexes: A New Approach to CuO Nanoparticles for Photocatalytic Degradation of Methylene Blue Dye," *Journal of Inorganic and Organometallic Polymers and Materials,* vol. 27, no. 5, pp. 1220-1233, 2017, doi: 10.1007/s10904-017-0569-x.

[47] G. Panthi, N. A. M. Barakat, M. Park, H.-Y. Kim, and S.-J. Park, "Fabrication of PdS/ZnS NPs doped PVAc hybrid electrospun nanofibers: Effective and reusable catalyst for dye photodegradation," *Journal of Industrial and Engineering Chemistry,* vol. 21, pp. 298-302, 2015, doi: 10.1016/j.jiec.2014.02.036.

[48] F. Würthner, "Perylene bisimide dyes as versatile building blocks for functional supramolecular architectures," *Chemical Communications,* no. 14, pp. 1564-1579, 2004, doi: 10.1039/B401630K.

[49] H. Langhals, "Color Chemistry. Synthesis, Properties and Applications of Organic Dyes and Pigments. 3rd revised edition. By Heinrich Zollinger," *Angewandte Chemie International Edition,* vol. 43, no. 40, pp. 5291-5292, 2004, doi: 10.1002/anie.200385122.

[50] A. R. Khataee and M. B. Kasiri, "Photocatalytic degradation of organic dyes in the presence of nanostructured titanium dioxide: Influence of the chemical structure of dyes," *Journal of Molecular Catalysis A: Chemical,* vol. 328, no. 1, pp. 8-26, 2010, doi: 10.1016/j.molcata.2010.05.023.

[51] A. Fujishima and K. Honda, "Electrochemical photolysis of water at a semiconductor electrode," (in eng), *Nature,* vol. 238, no. 5358, pp. 37-40, 1972, doi: 10.1038/238037a0.

[52] J. Schneider *et al.*, "Understanding TiO2 Photocatalysis: Mechanisms and Materials," *Chemical Reviews,* vol. 114, no. 19, pp. 9919-9986, 2014, doi: 10.1021/cr5001892.

[53] N. Serpone and A. V. Emeline, "Semiconductor Photocatalysis — Past, Present, and Future Outlook," *The Journal of Physical Chemistry Letters,* vol. 3, no. 5, pp. 673-677, 2012, doi: 10.1021/jz300071j.

[54] M. R. Hoffmann, S. T. Martin, W. Choi, and D. W. Bahnemann, "Environmental Applications of Semiconductor Photocatalysis," *Chemical Reviews,* vol. 95, no. 1, pp. 69-96, 1995, doi: 10.1021/cr00033a004.

[55] X. Chen and S. S. Mao, "Titanium Dioxide Nanomaterials: Synthesis, Properties, Modifications, and Applications," *Chemical Reviews,* vol. 107, no. 7, pp. 2891-2959, 2007, doi: 10.1021/cr0500535.

[56] K. P. Gopinath, N. V. Madhav, A. Krishnan, R. Malolan, and G. Rangarajan, "Present applications of titanium dioxide for the photocatalytic removal of pollutants from water: A review," *Journal of Environmental Management,* vol. 270, p. 110906, 2020, doi: 10.1016/j.jenvman.2020.110906.

[57] C. S. Turchi and D. F. Ollis, "Photocatalytic degradation of organic water contaminants: Mechanisms involving hydroxyl radical attack," *Journal of Catalysis,* vol. 122, no. 1, pp. 178-192, 1990, doi: 10.1016/0021-9517(90)90269-P.

[58] U. I. Gaya and A. H. Abdullah, "Heterogeneous photocatalytic degradation of organic contaminants over titanium dioxide: A review of fundamentals, progress and problems," *Journal of Photochemistry and Photobiology C: Photochemistry Reviews,* vol. 9, no. 1, pp. 1-12, 2008, doi: 10.1016/j.jphotochemrev.2007.12.003.

[59] J. Yao, H. Chen, F. Jiang, Z. Jiao, and M. Jin, "Titanium dioxide and cadmium sulfide co-sensitized graphitic carbon nitride nanosheets composite photocatalysts with superior performance in phenol degradation under visible-light irradiation," *Journal of Colloid and Interface Science,* vol. 490, pp. 154-162, 2017, doi: 10.1016/j.jcis.2016.11.051.

[60] M. N. Chong, B. Jin, C. W. K. Chow, and C. Saint, "Recent developments in photocatalytic water treatment technology: A review," *Water Research,* vol. 44, no. 10, pp. 2997-3027, 2010, doi: 10.1016/j.watres.2010.02.039.

[61] X. Wei *et al.*, "Facile in situ synthesis of plasmonic nanoparticles-decorated g-C3N4/TiO2 heterojunction nanofibers and comparison study of their photosynergistic effects for efficient photocatalytic H2 evolution," *Nanoscale,* vol. 8, no. 21, pp. 11034-11043, 2016, doi: 10.1039/C6NR01491G.

[62] V. Etacheri, C. Di Valentin, J. Schneider, D. Bahnemann, and S. C. Pillai, "Visible-light activation of TiO2 photocatalysts: Advances in theory and experiments," *Journal of Photochemistry and Photobiology C: Photochemistry Reviews,* vol. 25, pp. 1-29, 2015, doi: 10.1016/j.jphotochemrev.2015.08.003.

[63] M. Nasr, C. Eid, R. Habchi, P. Miele, and M. Bechelany, "Recent Progress on Titanium Dioxide Nanomaterials for Photocatalytic Applications," *ChemSusChem,* vol. 11, no. 18, pp. 3023-3047, 2018, doi: 10.1002/cssc.201800874.

[64] C. D. Dimitrakopoulos and P. R. L. Malenfant, "Organic Thin Film Transistors for Large Area Electronics," *Advanced Materials,* vol. 14, no. 2, pp. 99-117, 2002, doi: 10.1002/1521-4095(20020116)14:2<99::AID-ADMA99>3.0.CO;2-9.

[65] M. P. O'Neil, M. P. Niemczyk, W. A. Svec, D. Gosztola, G. L. Gaines, and M. R. Wasielewski, "Picosecond Optical Switching Based on Biphotonic Excitation of an Electron Donor-Acceptor-Donor Molecule," *Science,* vol. 257, no. 5066, pp. 63-65, 1992, doi: 10.1126/science.257.5066.63.

[66] F. Würthner, C. R. Saha-Möller, B. Fimmel, S. Ogi, P. Leowanawat, and D. Schmidt, "Perylene Bisimide Dye Assemblies as Archetype Functional Supramolecular Materials," *Chemical Reviews,* vol. 116, no. 3, pp. 962-1052, 2016, doi: 10.1021/acs.chemrev.5b00188.

[67] D. Görl, X. Zhang, and F. Würthner, "Molecular Assemblies of Perylene Bisimide Dyes in Water," *Angewandte Chemie International Edition,* vol. 51, no. 26, pp. 6328-6348, 2012, doi: 10.1002/anie.201108690.

[68] J. Yuenyongsuwan, N. Nithiyakorn, P. Sabkird, E. A. O'Rear, and T. Pongprayoon, "Surfactant effect on phase-controlled synthesis and photocatalyst property of TiO2 nanoparticles," *Materials Chemistry and Physics,* vol. 214, pp. 330-336, 2018, doi: 10.1016/j.matchemphys.2018.04.111.

[69] J.-Y. Zheng *et al.*, "The Effect of Surfactants on the Diameter and Morphology of Electrospun Ultrafine Nanofiber," *Journal of Nanomaterials,* vol. 2014, p. 689298, 2014, doi: 10.1155/2014/689298.

[70] H. Chen *et al.*, "Electrospun chitosan-graft-poly (ε-caprolactone)/poly (ε-caprolactone) nanofibrous scaffolds for retinal tissue engineering," *Int J Nanomedicine,* vol. 6, pp. 453-461, 2011, doi: 10.2147/IJN.S17057.

[71] J. Yin and L. Xu, "Batch preparation of electrospun polycaprolactone/chitosan/aloe vera blended nanofiber membranes for novel wound dressing," *International Journal of Biological Macromolecules,* vol. 160, pp. 352-363, 2020, doi: 10.1016/j.ijbiomac.2020.05.211.

[72] Y. Guo, D. He, S. Xia, X. Xie, X. Gao, and Q. Zhang, "Preparation of a Novel Nanocomposite of Polyaniline Core Decorated with Anatase-TiO2 Nanoparticles in Ionic Liquid/Water Microemulsion," *Journal of Nanomaterials,* vol. 2012, p. 202794, 2012, doi: 10.1155/2012/202794.

[73] I. Corazzari *et al.*, "Advanced physico-chemical characterization of chitosan by means of TGA coupled on-line with FTIR and GCMS: Thermal degradation and water adsorption capacity," *Polymer Degradation and Stability,* vol. 112, pp. 1-9, 2015, doi: 10.1016/j.polymdegradstab.2014.12.006.

[74] G. Sivalingam, R. Karthik, and G. Madras, "Kinetics of thermal degradation of poly(ε-caprolactone)," *Journal of Analytical and Applied Pyrolysis,* vol. 70, no. 2, pp. 631-647, 2003, doi: 10.1016/S0165-2370(03)00045-7.

[75] K. Fukushima, D. Tabuani, and G. Camino, "Nanocomposites of PLA and PCL based on montmorillonite and sepiolite," *Materials Science and Engineering: C,* vol. 29, no. 4, pp. 1433-1441, 2009, doi: 10.1016/j.msec.2008.11.005.

[76] S. Ramasundaram *et al.*, "Photocatalytic applications of paper-like poly(vinylidene fluoride)–titanium dioxide hybrids fabricated using a combination of electrospinning and electrospraying," *Journal of Hazardous Materials,* vol. 285, pp. 267-276, 2015, doi: 10.1016/j.jhazmat.2014.12.004.

[77] E. G. Bajsić, B. Mijović, N. V. Penava, T. H. Grgurić, M. Slouf, and E. Zdraveva, "The effect of UV irradiation on the electrospun PCL/TiO2 composites fibers," *Journal of Applied Polymer Science,* vol. 133, no. 24, 2016, doi: 10.1002/app.43539.

[78] M. Sudhakaran, S. Shabin, N. S, and S. Jagadeeshan, "Fabrication and characterization of electrospun poly(ε-caprolactone) / TiO2 nanocomposite membranes with synergistic antibacterial property with gentamicin against MRSA," *International Journal of Scientific and Engineering Research,* vol. 6, pp. 1638–1647, 2015.

[79] M. Tominac Trcin *et al.*, "Poly(ε-caprolactone) Titanium Dioxide and Cefuroxime Antimicrobial Scaffolds for Cultivation of Human Limbal Stem Cells," *Polymers*, vol. 12, no. 8*,* p. 1758doi: 10.3390/polym12081758.

[80] X. Gu *et al.*, "Three-component antibacterial membrane of poly(butylene carbonate), poly(lactic acid) and chitosan prepared by electrospinning,"

Materials Technology, vol. 34, no. 8, pp. 463-470, 2019, doi: 10.1080/10667857.2019.1576822.

[81] A. S. Kiran, T. S. S. Kumar, R. Sanghavi, M. Doble, and S. Ramakrishna, "Antibacterial and Bioactive Surface Modifications of Titanium Implants by PCL/TiO2 Nanocomposite Coatings," *Nanomaterials*, vol. 8, no. 10, doi: 10.3390/nano8100860.

[82] K. S. Lee, N. Ivanova, V. M. Starov, N. Hilal, and V. Dutschk, "Kinetics of wetting and spreading by aqueous surfactant solutions," *Advances in Colloid and Interface Science,* vol. 144, no. 1, pp. 54-65, 2008, doi: 10.1016/j.cis.2008.08.005.

[83] M. Thommes *et al.*, "Physisorption of gases, with special reference to the evaluation of surface area and pore size distribution (IUPAC Technical Report)," *Pure and Applied Chemistry,* vol. 87, no. 9-10, pp. 1051-1069, 2015, doi: 10.1515/pac-2014-1117.

[84] M. Faraldos and C. Goberna, "Area superficial, textura y distribucion porosa," in *Técnicas de analisis y caracterización de materiales*, 2 ed. Madrid: Consejo Superior de Investigaciones científicas, 2002, ch. 15, pp. 623-638.

[85] S. Haider *et al.*, "Adsorption kinetic and isotherm of methylene blue, safranin T and rhodamine B onto electrospun ethylenediamine-grafted-polyacrylonitrile nanofibers membrane," *Desalination and Water Treatment,* vol. 55, no. 6, pp. 1609-1619, 2015, doi: 10.1080/19443994.2014.926840.

[86] H. N. Tran, S.-J. You, A. Hosseini-Bandegharaei, and H.-P. Chao, "Mistakes and inconsistencies regarding adsorption of contaminants from aqueous solutions: A critical review," *Water Research,* vol. 120, pp. 88-116, 2017, doi: 10.1016/j.watres.2017.04.014.

[87] J.-Z. Zhang, "Avoiding spurious correlation in analysis of chemical kinetic data," *Chemical Communications,* vol. 47, no. 24, pp. 6861-6863, 2011, doi: 10.1039/C1CC11278C.

[88] M. Badertscher and E. Pretsch, "Bad results from good data," *TrAC Trends in Analytical Chemistry,* vol. 25, no. 11, pp. 1131-1138, 2006, doi: 10.1016/j.trac.2006.09.003.

[89] T. R. Sahoo and B. Prelot, "Chapter 7 - Adsorption processes for the removal of contaminants from wastewater: the perspective role of nanomaterials and nanotechnology," in *Nanomaterials for the Detection*

and Removal of Wastewater Pollutants, B. Bonelli, F. S. Freyria, I. Rossetti, and R. Sethi Eds.: Elsevier, 2020, pp. 161-222.

[90] W. J. Weber and E. H. Smith, "Simulation and design models for adsorption processes," *Environmental Science & Technology,* vol. 21, no. 11, pp. 1040-1050, 1987, doi: 10.1021/es00164a002.

[91] I. D. Mall, V. C. Srivastava, N. K. Agarwal, and I. M. Mishra, "Removal of congo red from aqueous solution by bagasse fly ash and activated carbon: Kinetic study and equilibrium isotherm analyses," *Chemosphere,* vol. 61, no. 4, pp. 492-501, 2005, doi: 10.1016/j.chemosphere.2005.03.065.

[92] N. Kannan and M. M. Sundaram, "Kinetics and mechanism of removal of methylene blue by adsorption on various carbons—a comparative study," *Dyes and Pigments,* vol. 51, no. 1, pp. 25-40, 2001, doi: 10.1016/S0143-7208(01)00056-0.

[93] V. J. P. Poots, G. McKay, and J. J. Healy, "Removal of Basic Dye from Effluent Using Wood as an Adsorbent," *Journal of Water Pollution Control Federation,* vol. 50, pp. 926-935, 1978.

[94] S. J. Allen, G. McKay, and K. Y. H. Khader, "Intraparticle diffusion of a basic dye during adsorption onto sphagnum peat," *Environmental Pollution,* vol. 56, no. 1, pp. 39-50, 1989, doi: 10.1016/0269-7491(89)90120-6.

[95] D. F. Ollis, "Kinetics of Photocatalyzed Reactions: Five Lessons Learned," (in English), *Frontiers in Chemistry,* Perspective vol. 6, 2018, doi: 10.3389/fchem.2018.00378.

[96] Y. Ma and J.-n. Yao, "Photodegradation of Rhodamine B catalyzed by TiO2 thin films," *Journal of Photochemistry and Photobiology A: Chemistry,* vol. 116, no. 2, pp. 167-170, 1998, doi: 10.1016/S1010-6030(98)00295-0.

[97] C. Guo, J. Xu, Y. He, Y. Zhang, and Y. Wang, "Photodegradation of rhodamine B and methyl orange over one-dimensional TiO2 catalysts under simulated solar irradiation," *Applied Surface Science,* vol. 257, no. 8, pp. 3798-3803, 2011, doi: 10.1016/j.apsusc.2010.11.152.

[98] C. Chen, W. Ma, and J. Zhao, "Semiconductor-mediated photodegradation of pollutants under visible-light irradiation," *Chemical Society Reviews,* vol. 39, no. 11, pp. 4206-4219, 2010, doi: 10.1039/B921692H.

[99] J. Alvarez-Ramirez, R. Femat, M. Meraz, and C. Ibarra-Valdez, "Some remarks on the Langmuir–Hinshelwood kinetics," *Journal of Mathematical Chemistry,* vol. 54, no. 2, pp. 375-392, 2016, doi: 10.1007/s10910-015-0566-7.

[100] K. V. Kumar, K. Porkodi, and F. Rocha, "Langmuir–Hinshelwood kinetics – A theoretical study," *Catalysis Communications,* vol. 9, no. 1, pp. 82-84, 2008, doi: 10.1016/j.catcom.2007.05.019.

[101] L. Lou, J. Wang, Y. J. Lee, and S. S. Ramkumar, "Visible Light Photocatalytic Functional TiO2/PVDF Nanofibers for Dye Pollutant Degradation," *Particle & Particle Systems Characterization,* vol. 36, no. 9, p. 1900091, 2019, doi: 10.1002/ppsc.201900091.

[102] M. F. Elkady and H. S. Hassan, "Photocatalytic Degradation of Malachite Green Dye from Aqueous Solution Using Environmentally Compatible Ag/ZnO Polymeric Nanofibers," *Polymers*, vol. 13, no. 13*,* p. 2033doi: 10.3390/polym13132033.

[103] B. Burton, D. Alexander, and H. Klein, "Epoxy formulations using Jeffamine polyether-amines," *Hunstman,* pp. 1-63, 2011.

[104] D. C. Northrop, O. Simpson, and N. F. Mott, "Electronic properties of aromatic hydrocarbons I. Electrical conductivity," *Proceedings of the Royal Society of London. Series A. Mathematical and Physical Sciences,* vol. 234, no. 1196, pp. 124-135, 1956, doi: 10.1098/rspa.1956.0020.

[105] L. Jia and X.-h. Qin, "The effect of different surfactants on the electrospinning poly(vinyl alcohol) (PVA) nanofibers," *Journal of Thermal Analysis and Calorimetry,* vol. 112, no. 2, pp. 595-605, 2013, doi: 10.1007/s10973-012-2607-9.

[106] N. Amariei, L. R. Manea, A. P. Bertea, A. Bertea, and A. Popa, "The Influence of Polymer Solution on the Properties of Electrospun 3D Nanostructures," *IOP Conference Series: Materials Science and Engineering,* vol. 209, no. 1, p. 012092, 2017, doi: 10.1088/1757-899X/209/1/012092.

[107] J. Hu, M. P. Prabhakaran, X. Ding, and S. Ramakrishna, "Emulsion electrospinning of polycaprolactone: influence of surfactant type towards the scaffold properties," *Journal of Biomaterials Science, Polymer Edition,* vol. 26, no. 1, pp. 57-75, 2015, doi: 10.1080/09205063.2014.982241.

[108] D. Ding *et al.*, "Piezo-photocatalytic flexible PAN/TiO2 composite nanofibers for environmental remediation," *Science of The Total Environment,* vol. 824, p. 153790, 2022, doi: 10.1016/j.scitotenv.2022.153790.

[109] Y. Ma *et al.*, "Adsorption and Visible Light Photocatalytic Degradation of Electrospun PAN@W18O49 Nanofibers," *Chemical Research in Chinese Universities,* vol. 37, no. 3, pp. 428-435, 2021, doi: 10.1007/s40242-020-0357-y.

[110] P. Teng *et al.*, "Flexible PAN-BiOI-AgI heterojunction nanofiber and the photocatalytic degradation property," *Opt. Mater. Express,* vol. 12, no. 3, pp. 1031-1042, 2022, doi: 10.1364/OME.450592.

[111] G. Panthi, K. R. Gyawali, and M. Park, "Towards the Enhancement in Photocatalytic Performance of Ag3PO4 Nanoparticles through Sulfate Doping and Anchoring on Electrospun Nanofibers," *Nanomaterials*, vol. 10, no. 5*,* doi: 10.3390/nano10050929.

[112] Z. Huang *et al.*, "Electrospun graphene oxide/MIL-101(Fe)/poly(acrylonitrile-co-maleic acid) nanofiber: A high-efficient and reusable integrated photocatalytic adsorbents for removal of dye pollutant from water samples," *Journal of Colloid and Interface Science,* vol. 597, pp. 196-205, 2021, doi: 10.1016/j.jcis.2021.04.020.

[113] F. Sun *et al.*, "Core-sheath structured TiO2@PVDF/PAN electrospun membranes for photocatalysis and oil-water separation," *Polymer Composites,* vol. 41, no. 3, pp. 1013-1023, 2020, doi: 10.1002/pc.25433.

[114] P. Pascariu, C. Cojocaru, P. Samoila, N. Olaru, A. Bele, and A. Airinei, "Novel electrospun membranes based on PVDF fibers embedding lanthanide doped ZnO for adsorption and photocatalytic degradation of dye organic pollutants," *Materials Research Bulletin,* vol. 141, p. 111376, 2021, doi: 10.1016/j.materresbull.2021.111376.

[115] A. Gupta, N. Khosla, V. Govindasamy, A. Saini, K. Annapurna, and S. R. Dhakate, "Trimetallic composite nanofibers for antibacterial and photocatalytic dye degradation of mixed dye water," *Applied Nanoscience,* vol. 10, no. 11, pp. 4191-4205, 2020, doi: 10.1007/s13204-020-01540-6.

[116] P. Pascariu, L. Olaru, A. L. Matricala, and N. Olaru, "Photocatalytic activity of ZnO nanostructures grown on electrospun CAB ultrafine fibers," *Applied Surface Science,* vol. 455, pp. 61-69, 2018, doi: 10.1016/j.apsusc.2018.05.119.